Discrete element analyses of a realistic-shaped rock block impacting against a soil buffering layer

Weigang Shen[1], Tao Zhao[1,2], Feng Dai[1*], Giovanni B. Crosta[3], Houzhen Wei[4]

[1] State Key Laboratory of Hydraulics and Mountain River Engineering, College of Water Resource and Hydropower, Sichuan University, Chengdu, 610065, China

[2] Department of Civil and Environmental Engineering, Brunel University London, London, UB8 3PH, United Kingdom

[3]Department of Earth and Environmental Sciences, Università degli Studi di Milano Bicocca, Piazza della Scienza 4, 20126 Milan, Italy

[4] State Key Laboratory of Geomechanics and Geotechnical Engineering, Institute of Rock and Soil Mechanics, Chinese Academy of Sciences, Wuhan 430071, China

* **Corresponding author:** Tel.: +86 28 8540 6701 E-mail: fengdai@scu.edu.cn

Abstract: This study is devoted to understanding the impact of irregularly-shaped rock blocks against a soil buffering layer above a rock shed via numerical simulations by discrete element method (DEM). In the DEM model, the rock block is represented by an assembly of densely packed and bonded spherical particles with the block shape reconstructed from the laser scanning results of a real rock block. The soil buffering layer is modeled as a loose packing of cohesionless frictional spherical particles, while the rock shed is simplified as a layer of fixed particles. The DEM model is firstly validated by modelling the impact of a cubic block against a soil buffering layer. Then, it is employed to investigate the dynamic interaction between a realistic-shaped rock block and the soil buffering layer. The numerical results show that the geometry of the contact surface between the rock block and soil layer can play a significant influence on the impact force of the rock block and the force acting on the rock shed. For the tested conditions, the distribution of stress on the rock shed can be well described by the Gaussian function, which seems to be independent on the geometry of the contact surface. In addition, the simplification of realistic-shaped rock blocks as spheres in traditional DEM modelling approaches can significantly underestimate of the impact force. The established modeling strategy serves as a starting point for investigating the rock block shape. The proposed results can contribute to the choice of buffering layer for designing the rock shed.

Keywords: irregular rock block; impact; soil buffering layer; discrete element method; impact force

1 Introduction

Rockfall is one of the most frequently occurring natural hazards in mountainous areas. It involves detachment of rock blocks from a steep slope or cliff and rapid downslope movements, which can induce significant risk to human lives, infrastructures and lifeline facilities because of the high kinetic energy and undefined trajectory (Crosta and Agliardi 2004). To mitigate such a hazard, rock sheds, embankments and retaining walls have been widely constructed (Volkwein et al. 2011; Lambert and Bourrier 2013). These protection systems generally consist of a load-carrying primary structure (e.g. concrete slab) and a granular buffering layer (usually soil or gravel) (Labiouse et al. 1996; Pichler et al. 2005; Lambert et al. 2009). The soil buffering layer plays a vital role in dissipating the impact energy of the falling rock block and reducing the impact pressure. Thus, a better understanding of the response of rock block impact against a soil buffering layer can contribute to an effective design of mitigating structures.

Over the past three decades, a large number of experimental and theoretical studies have been conducted to investigate the dynamic interaction between a rock block and a soil buffering layer (Labiouse et al. 1996; Calvetti et al. 2005; di Prisco and Vecchiotti 2006; Lambert et al. 2009; Calvetti and di Prisco 2012). In these studies, some important factors of the rock block impact process (e.g. buffering soil thickness, block mass and velocity) have been investigated intensively, aiming at producing scaling laws for the impact forces and penetration depth. Up to now, several empirical methods have been developed to estimate these quantities in engineering practice, such as the Chinese, Japanese and Swiss design codes (Ministry of Transport of the People's Republic of China 1995; Japan Road Association 2000; ASTRA 2008), in which the realistic rock block is simplified as an equal-volume sphere. In addition, numerical modelling using the discrete element method (DEM) (Cundall and Strack 1979) has also been used to analyze rock block impact from the microscopic to the macroscopic scale (Calvetti et al. 2005; Bourrier et al. 2010; Roethlin et al. 2013; Breugnot et al. 2016; Effeindzourou et al. 2017; Zhang et al. 2017a; Shen et al. 2019). With the help of DEM, the force chains evolution, energy transformation and dissipation of the soil layer have been analyzed in detail.

In the aforementioned studies, the rock block is consistently considered as a sphere, ellipsoid or cylinder. Actually, the shapes of real rock blocks can be highly irregular resembling cube, pyramid, prism, octahedron, wedge and disc (Fityus et al. 2013). In addition, several studies in the literature have indicated that the rock block shape has a great influence on its dynamics, impact force and the penetration depth (Degago et al. 2008; Glover et al. 2015; Breugnot et al. 2016; Gao and Meguid 2018a; Gao and Meguid 2018c; Yan et al. 2018; Shen et al. 2019). The experimental results of Degago et al. (2008) and the numerical results of Breugnot et al. (2016) show that a pyramidal block penetrates deeper than a spherical block. Shen et al. (2019) investigated the influence of block sphericity on the impact forces and penetration depth via the discrete element method (DEM). Their results illustrate that the impact force increases, while the penetration depth decreases linearly with the block sphericity. However, in these studies, the rock block is still simplified as a regular shape, failing to evaluate the effect of block morphology. Hence, more comprehensive analyses are needed to analyze the impact of a rock block against a soil layer by considering the real block shape.

The laser scanner (LS) method has been widely used to reconstruct the geometry of realistic rock blocks (Asahina and Taylor 2011; Wei et al. 2017; Paixão et al. 2018) by a workflow consisting of three steps. Firstly, a LS is used to generate a point cloud of the rock block. Then, the point cloud is cleaned by deleting erroneous points, reducing the number of points and filling voids. Finally, a triangular mesh, representing the block surface, is produced from the point cloud via a meshing algorithm. Based on the obtained mesh, the block can be constructed by the mathematical filling method (i.e. discrete element cluster method) in DEM (Shi et al. 2015; Wei et al. 2018; Zhou et al. 2018) which has been widely used to reconstruct irregular rock blocks and to investigate the effect of rock particle shape (Gao and Meguid 2018a; Gao and Meguid 2018b; Zhang et al. 2018). The corresponding results demonstrate the effectiveness of discrete element cluster method for modelling realistic-shaped rock blocks.

In the present study, the impact of a realistic-shaped rock block against a soil buffering layer has been investigated by discrete element modelling. The purpose is to establish a DEM model to quantify the impact of realistic-shaped rock blocks and evaluate the consequence of simplifying the real rock block as equal-volume sphere in engineering practice. The paper is organized as follows: Section 2 presents a brief introduction of the DEM theory. Section 3 illustrates the DEM model configurations and the reconstruction of a realistic-shaped rock block via the LS and discrete element cluster methods. Section 4 performs DEM model validation and a parametric study of realistic-shaped rock block. Section 5 discusses quantitatively the difference arising from the irregularity of rock block. Finally, some conclusions on the capability of DEM to model the rock block impact process are provided in Section 6.

2 Particle contact model

The open source DEM code ESyS-Particle (Weatherley et al. 2014) was used to run all the simulations presented in this study. This code has been widely employed to analyze the mechanical behavior of solids, such as soil and rock (Xu et al. 2015; Zhao et al. 2015; Guo and Zhao 2016; Liu et al. 2017; Shen et al. 2017; Zhao et al. 2017; Shen et al. 2018; Du et al. 2020). In the context of DEM, the materials are commonly mimicked as a collection of rigid spherical particles. The translational and rotational motions of each particle are governed by the Newton's second law of motion as:

$$F_i = m_i \frac{d^2}{dt^2} \boldsymbol{r_i} \tag{1}$$

$$M_i = I_i \frac{d^2}{dt^2} \boldsymbol{\omega_i} \tag{2}$$

where F_i is the resultant force acting on particle i; $\boldsymbol{r}_i$ is the position of its centroid; m_i is the particle mass; M_i is the resultant moment acting on the particle; $\boldsymbol{\omega}_i$ is the angular velocity and I_i is the moment of inertia.

The interactions between two contacting particles can be computed by the linear elastic spring-dashpot and parallel bond models for frictional and bonded contacts, respectively (Potyondy and Cundall 2004). For the frictional particle contact, the normal contact force (F_{n}) is calculated as,

$$F_{\mathrm{n}} = k_{\mathrm{n}} u_{\mathrm{n}} + F_{\mathrm{n}}^{\mathrm{d}} \tag{3}$$

where u_{n} is the overlapping distance between the two particles in contact; k_{n} is the normal contact stiffness and $F_{\mathrm{n}}^{\mathrm{d}}$ is the normal damping force. The normal contact stiffness is defined as $k_{\mathrm{n}} = \pi E_p \left(R_{\mathrm{A}} + R_{\mathrm{B}} \right) / 4$ with E_p being the particle Young's modulus, R_{A} and R_{B} being the radii of the two particles.

The normal damping force ($F_{\mathrm{n}}^{\mathrm{d}}$) is used to replicate energy dissipation induced by the plastic deformation of particles in the normal direction of contact, which can be calculated as,

$$F_{\mathrm{n}}^{\mathrm{d}} = -2\beta \sqrt{0.5\left(m_{\mathrm{A}} + m_{\mathrm{B}}\right) k_{\mathrm{n}}}\, v_{\mathrm{n}} \tag{4}$$

where β is the damping coefficient; m_{A} and m_{B} are the mass of the two contacting particles; v_{n} is the relative velocity between particles in the normal direction.

For the frictional particle contact, the tangential contact force at the current time step (F_s^n) is calculated incrementally as,

$$F_s^n = F_s^{n-1} + \left(\Delta F_{s1} + \Delta F_{s2} \right) \tag{5}$$

where $F_s^{n\text{-}1}$ is the tangential force at the previous iteration time step. ΔF_{s1} is calculated as $\triangle u_{\mathrm{s}} k_s$ with k_s being the tangential contact stiffness and $\triangle u_{\mathrm{s}}$ being the incremental tangential displacement. The tangential stiffness is calculated as $k_s = \pi E \left(R_A + R_B \right) / \left(8\left(1 + \upsilon\right)\right)$ with υ being the particle Poisson's ratio. ΔF_{s2} is the tangential force related to the rotation of particle contact plane. A detailed description of these two tangential force terms can be found in Wang and Mora (2009).

The magnitude of the tangential force is limited by the Coulomb's friction law as,

$$\left| F_{\mathrm{s}} \right| \le \mu \left| F_{\mathrm{n}} \right| \tag{6}$$

where μ is the friction coefficient of particle contact.

For the bonded particle contact, the interactions between two particles are calculated after Wang (2009) as:

$$F_{bn} = k_{bn} \cdot \Delta l_n \tag{7}$$

$$F_{bs} = k_{bs} \cdot \Delta l_s \tag{8}$$

$$M_b = k_b \cdot \Delta \alpha_b \qquad M_t = k_t \cdot \Delta \alpha_t \tag{9}$$

where F_{bn}, F_{bs} are the normal and tangential bonding forces; M_b and M_t are the bending and twisting moments, respectively. $k_{bn} = \pi E_b l_0 / 4$, $k_{bs} = \pi E_b l_0 / \left(8(1+\upsilon)\right)$, $k_b = \pi E_b l_0^3 / 64$ and $k_t = \pi E_b l_0^3 / \left(64(1+\upsilon)\right)$ are the corresponding bonding stiffness in the normal, tangential, bending and twisting directions, with E_b being the bond Young's modulus, υ being the Poisson's ratio. l_0 is the initial distance between particle centers. Δl_n, Δl_s, $\Delta \alpha_b$ and $\Delta \alpha_t$ are the relative displacements between the bonded particles in the normal, tangential, bending and twisting directions with respect to the initial particle positions.

The criterion of bond breakage is determined as follows:

$$\frac{F_{bn}}{F_{bnMax}} + \frac{F_{bs}}{F_{bsMax}} + \frac{M_b}{M_{bMax}} + \frac{M_t}{M_{tMax}} \geq 1 \tag{10}$$

where F_{bnMax}, F_{bsMax}, M_{bMax} and M_{tMax} are the maximum normal and shear bonding forces, bending and twisting moments, respectively. They can be calculated as $F_{bnMax} = \pi c l_0^2 / 4$, $F_{bnMax} = \pi c l_0^2 / 4$, $M_{bMax} = \pi c l_0^3 / 32$ and $M_{tMax} = \pi c l_0^3 / 16$, with c being the cohesive strength of the particle bond. In the present study, c is set to an extremely high value (e.g. 10^{20} MPa) to avoid the fragmentation of rock block during impact.

3 DEM model of rock block impact against soil layer

3.1 Modelling of realistic-shaped rock block

In this study, the realistic-shaped rock block is reconstructed via the laser scanner and discrete element cluster method (see Fig. 1). The LS apparatus PT-J200 (Wei et al. 2017) used to obtain the spatial coordinates of points on the exterior surface of rock block is shown in Fig. 1 (a). It has a scanning accuracy of 0.02 mm. The tested rock block (Fig. 1 (b1)) is an elongated limestone rock block. The longest, intermediate and shortest axis dimensions are 9.5 cm, 5.7 cm and 3.8 cm, respectively. This small rock block will be enlarged in the numerical simulations to represent large rock boulders generally observed in the field. The reason to choose such a rock block is that its shape is significantly different from a sphere, which is more realistic and helpful for the initial evaluation of the reliability of simplifying the real rock blocks as equal-volume sphere. The steps to reconstruct the realistic-shaped rock block are as follows: firstly, the LS apparatus is employed to obtain the point cloud of the rock block surface (Fig. 1 (b2)). Then, the cloud points are used to generate the triangular meshes for the actual geometry of rock block via the Delaunay triangulation method (Delaunay 1934) (Fig. 1 (b3)). Meanwhile, the meshes are enlarged to reach the block dimensions of 1.59 m, 0.95 m and 0.63 m in the longest, intermediate and shortest axis, respectively. Finally, the rock block is reconstructed by fitting spheres inside the triangular meshes using the random packing code GenGeo (Shao 2017). The reconstructed rock block is shown in Fig. 1 (b4).

3.2 Model configurations of rock block impact

The DEM model configurations of rock block impacting against a soil layer are shown in Fig. 2. In the DEM model, the soil layer is modeled as an assembly of cohesionless rigid spherical particles obtained by gravitational deposition. The layer, confined by four lateral walls and a layer of fixed particles (bottom floor), has dimensions of 2.1 m in thickness, 11.0 m in length and width. The fixed particles are used to represent the concrete slab, which ignores the deformation of bottom slab. The rock blocks tested in this study are presented in Fig. 3, including a cubic block (B-1), a realistic-shaped block (B-2) and its volume-equivalent sphere (B-3). The cubic block has a relatively larger mass than other blocks as it is chosen according to the experimental study of Pichler et al. (2005), so that the DEM model can be validated by comparing the numerical results of cube impact with their experimental results. To demonstrate the effect of rock block shape, the equal-volume spherical block (B-3) of the realistic-shaped rock block (B-2) has also been tested. The input parameters of the DEM model are listed in Table 1. The particles density in blocks B-1, B-2, B-3 are set differently so that the bulk density of these rock blocks is 2700 kg/m^3. The other parameters are the same as those in Shen et al. (2019). Due to the rotation of particles in the soil layer is inhibited, the friction angle of the granular soil is close to 45° (Calvetti 2008).

During the simulation, the rock block is positioned in the middle and just above the surface of the soil buffering layer. In the analysis, the block impacts against the soil layer with four different impact velocities (v_0), as summarized in Table 2. The cubic rock block collides onto the soil layer with a tip. To investigate the effect of rock block shape, the realistic-shaped rock block is used to impact vertically against the soil layer with different impact orientations, L^+, L^-, I^+, I^-, S^+ and S^-, respectively (see Fig. 3 (b) and Fig. 4). In fact, the cases of B-2-C1 and B-2-C2 can be considered as tip impact. The cases of B-2-C3, B-2-C4 and B-2-C5 can be considered as wedge impact. The case of B-2-C6 can be considered as face impact. Because the oblique impact is not the most detrimental situation, the oblique impact of rock blocks is not considered in this study. In addition, this study mainly focuses on the maximum impact force of the rock block and the maximum bottom force. Thus, the rotation of rock block after the initial impact has not been analyzed.

4 Results

In this study, the cubic rock block (B-1) is firstly tested (Sections 4.1) as a model validation against the experimental and theoretical results reported in Pichler et al. (2005). Then, the impact of realistic-shaped rock block (B-2) will be investigated in detail with respect to the impact force, the force chains, the bottom force and the bottom stress distribution (Sections 4.2–4.5). In addition, to evaluate the reliability of simplifying a real rock block as a sphere, the numerical results for B-2 have been compared with that for the equal-volume sphere impact (B-3).

4.1 DEM model validation

To verify whether the DEM model can mimic the impact of a rock block, a series of simulations are conducted with the cubic rock block (B-1). In these simulations, the rock block (B-1) impacts the soil layer by a tip with various impact velocities. The corresponding numerical results are analyzed and compared with the experimental and theoretical results in

Pichler et al. (2005) and Calvetti and di Prisco (2012). The main focus is on the evolution of impact force (F_{block}), the maximum impact force ($F_{block}^{\max}$) and the final penetration depth of the rock block ($Z_{block}^{\max}$).

Fig. 5 shows the evolution of the impact force of the rock block (B-1) in the experimental and numerical tests of h_f = 8.55 m. It can be seen that the numerical results can match well the experimental results. In particular, the numerical simulation can capture the characteristics of peak impact force in the experiment. In addition, the impact duration, defined as the time period over which the rock block encounters a significant impact force (i.e. > 0), is almost identical in the experimental and numerical tests.

According to Pichler et al. (2005), for a cubic rock block of volume (V) impacting against a soil layer with a tip at velocity (v_0), $Z_{block}^{\max}$ can be calculated as

$$Z_{block}^{\max} = d\left(\frac{103500h_f}{R+19180h_f}\right)^{1/2} \tag{11}$$

where d is the diameter of the equivalent projectile of the cubic rock block ($d = 1.05(V)^{1/3}$), R is the strength-like indentation resistance of soil buffering layer and h_f is the equivalent falling height of rock block ($h_f = v_0^2/2g$).

In addition, $F_{block}^{\max}$ and $Z_{block}^{\max}$ satisfy the following relationship,

$$\frac{mv_0^2}{F_{block}^{\max}d} = \frac{Z_{block}^{\max}}{d} \tag{12}$$

where m is the mass of the cubic rock block.

Therefore, according to Eqs. (11) and (12), $F_{block}^{\max}$ and $Z_{block}^{\max}$ can be estimated as,

$$F_{block}^{\max} = \frac{mv_0^2}{1.05(V)^{1/3}}\left(\frac{R+19180h_f}{103500h_f}\right)^{1/2} \tag{13}$$

$$Z_{block}^{\max} = 1.05(V)^{1/3}\left(\frac{103500h_f}{R+19180h_f}\right)^{1/2} \tag{14}$$

The comparison of the numerical results and the theoretical results of Eqs. (13) and (14) is shown in Fig. 6. It can be seen that both the maximum impact force ($F_{block}^{\max}$) and final penetration depth ($Z_{block}^{\max}$) increase with the equivalent falling height, due to the increasing impact velocity. In addition, the general increasing trends of $F_{block}^{\max}$ and $Z_{block}^{\max}$ can be well fitted by the theoretical formula (Eqs. (13) and (14)) with the indentation resistance of the soil layer in the DEM model equal to 1.07 × 10^7 Pa. This value of indentation resistance is close to the experimental ones found in Pichler et al. (2005) (ca. 4.58 × 10^6 - 1.86 × 10^7 Pa), indicating that the soil properties of the DEM sample used in this research can approximately match that of the gravel used in the experimental study of Pichler et al. (2005).

To verify if the DEM model can reproduce the interaction between the soil layer and the concrete slab, the impact process of a spherical rock block with diameter of 0.9 m and mass of 850 kg onto the soil layer at h_f = 36.5 m is simulated. The contact stress ($\Delta\sigma$) between the soil layer and the bottom floor center is computed and compared with the experimental results of Calvetti and di Prisco (2012). as shown in Fig. 7. The comparison between the impact force of this study and that of Calvetti and di Prisco (2012) has been detailed in Shen et al. (2019), which will not be repeated herein. As the bottom floor is fixed, the peak of the numerical result is 4.5% larger than that of the experimental result (see Fig. 7). In addition, $\Delta\sigma$ in the numerical simulation decreases to zero earlier than in the experiment. However, the general evolution pattern of $\Delta\sigma$ in the numerical simulation is the same as in the experiment.

Overall, the agreement between the numerical results and the experimental and theoretical results indicates that the DEM model can be used to investigate the impact of a rock block against a soil layer covering a concrete slab.

4.2 Impact force on the rock block

Fig. 8 presents the evolution of impact force (F_{block}) for the cases of a realistic rock block (B-2) impacting against the soil layer at different orientations (v_0 = 30 m/s). After colliding onto the soil layer, the impact force firstly increases to the peak value within a short time and then decreases gradually to zero. The impact duration is smaller than 0.05 s. The numerical results in Fig. 8 also show that the rock block shape has a great influence on the impact force and impact duration, due to the variation of the geometry of impact surface. For the test of rock block face impact (B-2-C6), the impact force is much larger and the impact duration is much shorter than other cases. For the test of tip impact (B-2-C1), the impact force becomes the smallest and the impact duration is the longest. The impact duration of B-3 is larger than that of B-2-C1, while it is smaller than other cases. According to Zhang et al. (2017b), this phenomenon is actually related to the number of soil particles (N_{bc}) contacting with the rock block and the force chains formed in the soil buffering layer at impact. In the current study, the evolution of N_{bc} is shown in Fig. 9. It can be seen that N_{bc} evolves similarly as the impact force. Once the rock block touches the soil layer, N_{bc} increases sharply to the peak in a short time. The time at which N_{bc} reaches the peak value is the same as that for the impact force. In addition, the maximum value of N_{bc} for the case of B-2-C6 is obviously larger than that for B-2-C1 and B-3. For face impact, the rock block can have more contacts with the soil particles. Therefore, these soil particles are less likely to be pushed laterally due to lateral confinement imposed by other stressed particles (Zhang et al. 2017b). Hence, the force chains in the soil buffering layer can maintain stable at interactions with the rock block, leading to greater impact force and shorter impact duration. On the contrary, for tip impact, the rock block has relatively small contact surface areas to the soil layer and the number of block-particle contacts is small. Thus, the number of force chains formed in the soil layer is relatively small, leading to smaller impact force and longer impact duration.

Fig. 10 presents the relationship between the maximum impact force ($F_{block}^{\max}$) and the impact velocity (v_0) for the realistic shaped rock block (B-2) and its equal-volume sphere (B-3). As expected, the results exhibit an increase of the maximum impact force with the impact velocity, due to the increase of kinetic energy at impact. At a given impact velocity, the maximum impact force depends significantly on the geometry of the impact surface. Generally, the maximum impact force of a face impact (i.e. B-2-C6) is larger than that of a tip impact (i.e. B-2-C1). In addition, as the impact velocity increases, the difference of maximum impact forces for the tests of different impact surfaces becomes more obvious. From Fig. 10, it can also be seen that the maximum impact force of the realistic-shaped rock block (B-2) is different from that of the corresponding equal-volume sphere (B-3) (e.g. the cases of B-2-C1 and B-2-C6). The maximum impact force B-2-C1 is smaller than that of B-3, while the maximum impact force of B-2-C6 is much larger than that of B-3. The ratios of the maximum impact force of B-2 to that of B-3 under condition of different impact velocities are listed in Table 3. For the tests of v_0 = 10.0 m/s, the maximum impact force of B-2-C6 is 1.71 times larger than that of B-3. As v_0 increases to 30.0 m/s, the maximum impact force of B-2-C6 can be 2.2 times that of B-3. The ratio of the maximum impact force of B-2 to that of B-3 is similar to the results of Breugnot et al. (2016), although the shape and mass of rock blocks tested are different. The current numerical results indicate that the irregularity of rock block has a significant influence on the impact force of rock block, especially for high-speed impacts. The maximum impact force of a realistic-shaped rock block can be quite larger than that of its equal-volume sphere. This is especially evident for the rock block impacting with a face.

4.3 Contact force chains and strain energy

The contact force chains formed in the soil layer at the time instant corresponding to the peak impact force for the realistic-shaped rock block impacting at v_0 = 30 m/s are presented in Fig. 11. Here, the force chain is defined as a network of discontinuous lines connecting the centers of particles in contact. The thickness of these lines is proportional to the magnitude of contact force. It can be seen that the force chains formed in the soil layer for the B-2-C6 simulation are more than for the case of B-2-C1. From Fig. 11, it can be seen that the confining effect by the surrounding particles is similar to that in a shallow foundation for different ratios between the foundation width and the thickness of the soil layer. In other words, a small contact area is similar to a point load where small number of horizontal force chains exist in the soil layer, while a large one tends to oedometric loading conditions where large number of horizontal force chains exist in the soil layer. From Fig. 11, it can also be seen that for the B-2-C1 case, the force wave has reached the bottom floor at the peak impact force time, because it takes a much longer time for the peak of impact force to be reached (see Fig. 8), giving time for the force wave to cross the layer. However, for the other cases, the force wave has not reached the bottom floor, in accordance with the experimental results of Calvetti and di Prisco (2012). This indicates that for the case of tip impact, the block-soil interaction can be affected by the bottom floor, while for the cases of wedge and face impact, the block-soil interaction is unaffected by the presence of the bottom floor.

The impact of rock block onto a granular layer also involves evolution and transformation of a series of energy components (Zhang et al. 2017a). During the impact, the kinetic energy of the rock block is gradually transferred into the soil buffering layer, inducing the increase of the kinetic energy of soil particles (E_{kl}) and strain energy (E_{sl}) stored at the particle contacts. The strain energy (E_{sl}) is highly related to the number and stability of force chains formed in the granular layer. The more stable the force chains are, the larger the strain energy, the more resistance the granular layer can give to the rock block. The evolutions of E_{kl} and E_{sl} for the tests of B-2 impacting onto the soil layer at h_{f} = 30.0 m/s is shown in Fig. 12. It is clear that E_{kl} and E_{sl} evolves similarly as the impact force. Once the rock block touches the soil layer, E_{kl} and E_{sl} increases sharply to the peak in a short time. The time at which E_{sl} reaches the peak value is the same as that for the impact force. In addition, it is obvious that the maximum strain energy and kinetic energy of B-2-C6 is larger than that of B-2-C1. This indicates that there are more stable force chains formed in the soil layer for the test of B-2-C6. For the test B-2-C6, the rock block encounters more resistance from the soil layer, which verifies the above discussion of the impact force.

4.4 Impact-induced bottom force

Fig. 13 shows the evolution of bottom force (F_{bott}) for the cases of B-2 impacting against the soil layer with different orientations. The bottom force is the result of the interaction between the bottom floor and the stress wave induced by the impact of the rock block (Calvetti et al. 2005). In the current analysis, F_{bott} is defined as the vertical component of the total contact force between the soil layer and the bottom floor. As shown in Fig. 13, for all tests, the increase of F_{bott} is delayed by 0.01 s due to the propagation of impact-induced stress wave within the soil buffering layer. This indicates that the propagation velocity of the stress wave within in the soil layer is 210 m/s, which is independent of the geometry of impact face. After t = 0.01 s, F_{bott} firstly increases quickly to the peak value, and then decreases to zero and eventually becomes negative. The negative value is due to the separation between the soil particles and the bottom floor, which has been detailed in Shen et al. (2019) and Zhang et al. (2017a). Even though the impact surface varies, the evolution pattern of the bottom force for the realistic-shaped rock block is the same as its equal-volume sphere. However, from Fig. 13, it can be seen that the geometry of impact surface influences the maximum positive bottom force significantly as well the rate of F_{bott} increase. The maximum bottom force ($F_{bott}^{\max}$) of a face impact (i.e. B-2-C6) is greater than that for the tip impact. In fact, this phenomenon is related to the number and stability of force chains formed in the soil layer (Zhang et al. 2017a; Su et al. 2018), because the buckling (instability) of force chain is associated with the energy dissipation of the granular layer. For the case of face impact, there are more force chains forming and more particles stressed in the soil layer (see Fig. 11). The force chains are more stable and less likely to buckle, leading to less energy dissipation. Thus, more strain energy can be transmitted by the force chains to the bottom force, leading to a larger bottom force.

The maximum bottom forces ($F_{bott}^{\max}$) for the tests on rock block (B-2) and its equal-volume sphere (B-3) are summarized in Fig. 14. The results show that $F_{bott}^{\max}$ increases with the impact velocity, which is in line with the increasing pattern of the maximum impact force. In addition, $F_{bott}^{\max}$ exhibits a clear dependence on the geometry of impact surface. Generally, the $F_{bott}^{\max}$ of face impact (i.e. B-2-C6) is larger than that of tip impact (e.g. B-2-C1), especially at a high impact velocity. From Fig. 14, it can also be seen that $F_{bott}^{\max}$ of the realistic-shaped rock block (B-2) is different from that for its equal-volume sphere (B-3). The maximum bottom force of B-2-C1 is smaller than that of B-3, while the maximum bottom force for the case of B-2-C6 is larger than that for B-3. The ratios of the maximum bottom force of B-2 to that of B-1 under different impact velocities are listed in Table 4. In addition, the ratio increases with the impact velocity. The maximum bottom force of the realistic-shaped rock block can be 1.49 times that of the corresponding equal-volume sphere.

By comparing Fig. 10 and Fig. 14, it can be found that the maximum bottom force ($F_{bott}^{\max}$) is larger than the maximum impact force ($F_{block}^{\max}$). This is due to the dynamic amplification of loading in the soil buffering layer which can lead to a maximum bottom force much larger than the corresponding maximum impact force (Calvetti et al. 2005). The ratio of $F_{bott}^{\max}$ to $F_{block}^{\max}$, defined as amplification ratio ($\alpha = F_{bott}^{\max} / F_{block}^{\max}$), has been widely used in engineering practice to estimate the bottom force (Japan Road Association 2000; ASTRA 2008). The amplification ratios for the tests of B-2 and B-3 impacting at various velocities are summarized in Fig. 15 and Table 5. The amplification ratio of sphere impact (B-3) is close to 2.0, which matches well the experimental and numerical results reported in the literature (Zhang et al. 2017a) where spherical rock blocks impacting onto a 2.0 m thickness layer were tested. However, it can be seen that the amplification ratio depends on the impact velocity and the geometry of impact surface. As the impact velocity increases, the amplification ratio decreases. This is because the impact force is more sensitive to the impact velocity in comparison with the bottom force (see Fig. 10 and Fig. 14). In addition, the amplification ratios of the realistic-shaped rock block are different from that of its equal-volume sphere. The amplification ratio of B-2-C1 is larger than that of B-3, while the amplification ratio of B-2-C6 is smaller than that of B-3. This is because the influence of the impact face on the impact force is more significant than on the bottom force (see Fig. 8 and Fig. 13).

4.5 Bottom stress distribution

The contact stress between the soil layer and the bottom floor is also important as it determines the deformation of concrete slab beneath the soil layer (Calvetti and di Prisco 2012). To analyze the bottom stress distribution, the bottom floor is mapped as a 11 × 11 element grid (see Fig. 16). The average normal stress (σ) at the i-th mesh cell is calculated as F_i/S_i, where F_i is the vertical component of the contact forces between the bottom floor and the soil particles and S_i is the area of the i-th mesh cell. For simplification, the normal stresses of the grid cells at the bottom center and along the X-axis and Y-axis of the bottom floor (grey meshes in Fig. 16) are evaluated. The distributions of maximum normal stresses ($\sigma_x^{\max}$) and ($\sigma_y^{\max}$) along X-axis and Y-axis are plotted in Fig. 17. It can be seen that the geometry of the impact has a significant influence on the peak of stress distribution. The peak of the stress distribution of face impact (B-2-C6) is larger than that of tip impact (B-2-C1). However, the impact surface has little influence on the distribution pattern of $\sigma_x^{\max}$ and $\sigma_y^{\max}$. The peak value occurring just at the bottom center (x = 0.0 and y = 0.0). $\sigma_x^{\max}$ and $\sigma_y^{\max}$ decreases with the distance from the bottom center. As the distance increases to 3 m, $\sigma_x^{\max}$ and $\sigma_y^{\max}$ decrease almost by 90% compared to the peak value. It is worth noting that the distribution of maximum normal stress is not axisymmetric due to the irregularity of impact surface, which means that the maximum stresses at cells of the same distance from the bottom center are different. This is evident for the test of B-2-C1. Even though an axisymmetric block is used (i.e. B-3), the distribution of maximum normal stress is not axisymmetric (see Fig. 17) due to the anisotropy of the soil layer. However, the numerical data can be well fitted by the Gaussian function as,

$$\sigma_x^{\max} = \sigma_0 + Ae^{-2\frac{(x-x_c)^2}{b^2}} \tag{15}$$

where σ_0 is the bottom asymptote of the fitting function; A is height of the curve's peak; x_c is the position of the center of the peak and b is standard deviation. As shown in Fig. 17, for tests of realistic-shaped rock block (B-2) impacting against the soil layer with various impact orientations, the numerical data match well with the Gaussian function (R^2 > 0.98). This indicates that the Gaussian function can be used to describe the stress distribution on the bottom floor induced by the impact of realistic-shaped rock blocks. It should be noted that this distribution is obtained by calculating the maximum stresses on each cell. However, the maximum stress acting on each cell occurs at different time. Theoretically, the central cell is the very first to reach the maximum stress, but when the maximum stress is reached on other cells, the stress in the central cell has diminished. Therefore, the bottom force calculated by the distribution of maximum normal stress is overestimated.

The maximum normal stresses ($\sigma_{x=0.0}^{\max}$) acting on the bottom center (x = 0.0 m) for B-2 and B-3 impacting at various velocities are presented in Fig. 18. The numerical results show that $\sigma_{x=0.0}^{\max}$ exhibits a clear dependence on the impact velocity and orientation. For all the tests of B-2 and B-3, $\sigma_{x=0.0}^{\max}$ increases with the impact velocity. For a given impact velocity, $\sigma_{x=0.0}^{\max}$ varies with the geometry of impact orientation. $\sigma_{x=0.0}^{\max}$ for face impact (B-2-C6) is larger than that of tip impact (B-2-C1), this becoming more and more obvious as the impact velocity increases. In addition, $\sigma_{x=0.0}^{\max}$ of a realistic-shaped rock block can be very different from its equal-volume sphere. Generally, $\sigma_{x=0.0}^{\max}$ of face impact (B-2-C6) is larger than that of the equal-volume sphere (B-3), while $\sigma_{x=0.0}^{\max}$ of tip impact (B-2-C1) is smaller than that for B-3. In particular, for high-speed impact, $\sigma_{x=0.0}^{\max}$ of realistic-shaped rock block can be 2.0 times as that for the equal-volume sphere impact.

Fig. 19 shows the relationship between $\sigma_{x=0.0}^{\max}$ and $F_{block}^{\max}$ for tests of B-2 and B-3 impacting against the soil layer at different velocities. Although the geometry of impact surface varies, $\sigma_{x=0.0}^{\max}$ increases linearly with the maximum impact force ($F_{block}^{\max}$). The slope of the fitting line is 0.23, which is the same as the data reported in Shen et al. (2019). This indicates that $\sigma_{x=0.0}^{\max}$ can be estimated via multiplying $F_{block}^{\max}$ by a unique coefficient which is independent of the impact velocity, the rock block shape and mass at least for a simplified layer. This coefficient appears to be an intrinsic property of the soil buffering layer even if we only tested a limited set of conditions. Hence, this coefficient can be evaluated by using spherical rock block impact test for estimating the bottom center stress of realistic-shaped rock block impacts. Once the maximum stress on the center is estimated, the maximum stress distribution could be obtained based on the Gaussian function. Thus, the concrete slab can be designed based on the maximum stress distribution.

5 Discussion

In the literature, many researchers have conducted a lot of experimental and numerical studies to investigate the impact of spherical projectile onto a granular bed (Katsuragi and Durian 2007; Katsuragi and Durian 2013; Kang et al. 2018). The corresponding results indicate that the impact force of a sphere can be interpreted by the generalized Poncelet force law (Katsuragi and Durian 2007). It involves a depth-dependent force term induced by inter-particle friction and a velocity-dependent force term arising from the projectile-particle collision. The depth-dependent force depends on the volume of particles displaced by the projectile, which is similar to the Archimedes' law (Kang et al. 2018). The velocity-dependent force is related to the impact face (Katsuragi and Durian 2013). The larger the area of impact face is, the larger the velocity-dependent force will be. In this study, penetrating volume (PV) is defined to quantify the difference between various impact cases. PV is calculated as the volume of rock block immersed in the soil layer when assuming that the penetration depth has reached one-tenth of the diameter of the equal-volume sphere (B-3) (see Fig. 20). Therefore, larger the penetrating volume (PV) means the larger impact face area and volume of particles displaced by the projectile. This will lead to larger impact force. The penetrating volumes of B-2 and B-3 are calculated and summarized in Fig. 20. It is clear that the PV of B-2-C6 is obviously larger than that of B-3. Hence, the impact force of B-2-C6 is larger than that of B-3. On the contrary, due to the smaller PV, the impact force of B-2-C1 is smaller than that of B-3. The PV for other cases (i.e. B-2-C2, B-2-C3, B-2-C4, and B-2-C5) are close to each other. Hence, the impact force for these cases are close to one another. In addition, the numerical results illustrate that the maximum bottom force increases with the penetration volume. The testing case of B-2-C3 is an exception, because the impact has induced the rotation of the block due to the highly asymmetrical impact area (see Fig. 20).

6 Conclusions

This study established a numerical model to quantify the impact of a realistic-shaped rock block against a soil buffering layer via the discrete element method. The realistic-shaped rock block is reconstructed by the laser scanner and the discrete element cluster methods. The numerical model was first validated, and then used to investigate the mechanical response of realistic-shaped rock block impact. A series of simulations for the realistic-shaped rock block impacting onto the soil layer with various impact surfaces and velocities have been conducted. The corresponding numerical results have been compared with that for the equal-volume spherical block of the realistic-shaped rock block which is a common assumption used in many studies.

The obtained numerical results illustrate that the irregularity of realistic-shaped rock blocks can lead to three kinds of impacts, namely the tip, edge and face impacts. The geometry of the contact surface between the rock block and the soil layer influences the impact force, the bottom force and the bottom center stress significantly. The face impact results in short impact duration and large maximum impact force, bottom force and bottom center stress. The amplification ratio of the soil layer also exhibits a clear dependence on the geometry of impact orientation. However, the geometry of contact surface has little influence on the distribution of peak stress on the bottom floor, which can be well described by the Gaussian distribution function. In addition, the peak stress at the bottom center correlates linearly with the maximum impact force. The ratio of the peak stress at the bottom center to the maximum impact force is independent of the impact velocity and the geometry of contact surface. The numerical results also indicate that the simplification of the realistic-shaped rock block as equal-volume sphere can underestimate of the maximum impact force (i.e. 2 times), especially for high-speed rock block impact. The established numerical model and the results obtained in this study can give some new insights into the designing practices of effective soil buffering layers for rockfall hazards mitigations.

It should be noted that the numerical model employed in this study was calibrated based on a specific soil layer. The influence of soil characteristics (friction angle, compaction, fabric and diffusion angle) on the impact force and load distribution on the slab were not investigated. At the same time, the concrete slab is perfectly rigid and positioned at a fixed depth. Therefore, someone who would like to use the numerical model and results of this study in engineering practices should firstly carefully verify the soil characteristics.

Acknowledgements

This research was supported by the National Natural Science Foundation of China (grant

51779164, 41602289 and 41877260), the open funding of the State Key Laboratory of Hydraulics and Mountain River Engineering (Sichuan University) (No. Skhl1808) and the @RockHoriZon advanced tools for rockfall hazard and risk zonation at the regional scale (Grant 2016–0756), Fondazione CARIPLO.

References

Asahina D, Taylor MA (2011) Geometry of irregular particles: Direct surface measurements by 3-D laser scanner. Powder Technol 213(1): 70-78.

ASTRA (2008) Actions de chutes de pierres sur les galeries de protection. Office fédéral des routes OFROU.

Bourrier F, Nicot F, Darve F (2010) Evolution of the micromechanical properties of impacted granular materials. Comptes Rendus Mecanique 338: 639-647.

Breugnot A, Lambert S, Villard P, Gotteland P (2016) A Discrete/continuous Coupled Approach for Modeling Impacts on Cellular Geostructures. Rock Mech Rock Eng 49(5): 1831-1848.

Calvetti F (2008) Discrete modelling of granular materials and geotechnical problems. Eur J Envron Civ Eng 12: 951-965.

Calvetti F, di Prisco C (2012) Rockfall impacts on sheltering tunnels: Real-scale experiments. Géotechnique 62(10): 865-876.

Calvetti F, di Prisco C, Vecchiotti M (2005) Experimental and numerical study of rock-fall impacts on granular soils. Riv Ital Geotec 4: 95-109.

Crosta GB, Agliardi F (2004) Parametric evaluation of 3D dispersion of rockfall trajectories. Nat Hazards Earth Syst Sci 4(4): 583-598.

Cundall PA, Strack ODL (1979) A discrete numerical model for granular assemblies. Géotechnique 29(1): 47– 65.

Degago S, Ebeltoft R, Nordal S (2008) Effect of Rock Fall Geometries Impacting Soil Cushion: A Numerical Procedure. The 12th International Conference of International Association for Computer Methods and Advances in Geomechanics, India.

Delaunay B (1934) Sur la sphère vide. A la mémoire de Georges Voronoï. Bulletin de l'Académie des Sciences de l'URSS 6: 793-800.

di Prisco C, Vecchiotti M (2006) A rheological model for the description of boulder impacts on granular strata. Géotechnique 56(7): 469-482.

Du H-b, Dai F, Xu Y, Yan Z, Wei M-d (2020) Mechanical responses and failure mechanism of hydrostatically pressurized rocks under combined compression-shear impacting. International Journal of Mechanical Sciences 165: 105219.

Effeindzourou A, Giacomini A, Thoeni K, Sloan SW (2017) Numerical Investigation of Rockfall Impacts on Muckpiles for Underground Portals. Rock Mech Rock Eng 50(6): 1569-1583.

Fityus SG, Giacomini A, Buzzi O (2013) The significance of geology for the morphology of potentially unstable rocks. Eng Geol 162: 43-52.

Gao G, Meguid M (2018a) Modeling the Impact of a Falling Rock Cluster on Rigid Structures. Int J Geomech 18(2): 1-15.

Gao G, Meguid MA (2018b) Effect of particle shape on the response of geogrid-reinforced systems: Insights from 3D discrete element analysis. Geotext Geomembr 46(6): 685-698.

Gao G, Meguid MA (2018c) On the role of sphericity of falling rock clusters—insights from experimental and numerical investigations. Landslides 15(2): 219-232.

Glover J, Bartelt P, Christen M, Gerber W (2015). Rockfall-Simulation with Irregular Rock Blocks.*In*: Lollino, G. (ed.) *Engineering Geology for Society and Territory - Volume 2*. Springer International Publishing, Cham, 1729-1733.

Guo N, Zhao J (2016) 3D multiscale modeling of strain localization in granular media. Comput Geotech 80: 360-372.

Japan Road Association (2000) Manual for Anti-impact Structures Against Falling Rocks, Japan.

Kang W, Feng Y, Liu C, Blumenfeld R (2018) Archimedes' law explains penetration of solids into granular media. Nature Communications 9(1): 1101.

Katsuragi H, Durian DJ (2007) Unified force law for granular impact cratering. Nature Physics 3(6): 420-423.

Katsuragi H, Durian DJ (2013) Drag force scaling for penetration into granular media.

Physical Review E 87(5): 052208.

Labiouse V, Descoeudres F, Montani S (1996) Experimental study of rock sheds impacted by rock blocks. Struct Eng Int 3(3): 171-176.

Lambert S, Bourrier F (2013) Design of rockfall protection embankments: A review. Eng Geol 154: 77-88.

Lambert S, Gotteland P, Nicot F (2009) Experimental study of the impact response of geocells as components of rockfall protection embankments. Nat Hazards Earth Syst Sci 9(2): 459-467.

Liu Y, Dai F, Zhao T, Xu N-w (2017) Numerical Investigation of the Dynamic Properties of Intermittent Jointed Rock Models Subjected to Cyclic Uniaxial Compression. Rock Mech Rock Eng 50(1): 89-112.

Ministry of Transport of the People's Republic of China (1995) Specifications for Design of Highway Subgrades (JTJ013-95).

Paixão A, Resende R, Fortunato E (2018) Photogrammetry for digital reconstruction of railway ballast particles – A cost-efficient method. Constr Build Mater 191: 963-976.

Pichler B, Hellmich C, Mang HA (2005) Impact of rocks onto gravel Design and evaluation of experiments. Int J Impact Eng 31(5): 559-578.

Potyondy DO, Cundall PA (2004) A bonded-particle model for rock. Int. J Rock Mech Min Sci 41(8): 1329-1364.

Roethlin C, Calvetti F, Yamaguchi S, Vogel T (2013) Numerical simulation of rockfall impact on a rigid reinforced concrete slab with a cushion layer. Fourth International Workshop on Performance, Protection and Strengthening of Structures, Mysore, India.

Shao Q (2017) ESyS-Particle gengeo-1.4. World Wide Web Address: https://launchpad.net/esys-particle/+milestone/gengeo-1.4.

Shen W, Zhao T, Dai F, Jiang M, Zhou GGD (2019) DEM analyses of rock block shape effect on the response of rockfall impact against a soil buffering layer. Eng Geol 249: 60-70.

Shen W, Zhao T, Zhao J, Dai F, Zhou GGD (2018) Quantifying the impact of dry debris flow against a rigid barrier by DEM analyses. Eng Geol 241: 86-96.

Shen WG, Zhao T, Crosta GB, Dai F (2017) Analysis of impact-induced rock fragmentation using a discrete element approach. Int J Rock Mech Min Sci 98: 33-38.

Shi C, Li D-j, Xu W-y, Wang R (2015) Discrete element cluster modeling of complex mesoscopic particles for use with the particle flow code method. Granul Matter 17(3): 377-387.

Su Y, Cui Y, Ng CWW, Choi CE, Kwan JSH (2018) Effects of particle size and cushioning thickness on the performance of rock-filled gabions used in protection against boulder impact. Can Geotech J 56(2): 198-207.

Volkwein A, Schellenberg K, Labiouse V, Agliardi F, Berger F, Bourrier F, Dorren L, Gerber W, Jaboyedoff M (2011) Rockfall characterisation and structural protection – a review. Nat Hazards Earth Syst Sci 11(9): 2617-2651.

Wang Y (2009) A new algorithm to model the dynamics of 3-D bonded rigid bodies with rotations. Acta Geotechnica 4(2): 117-127.

Wang Y, Mora P (2009). The ESyS_Particle: A New 3-D Discrete Element Model with Single Particle Rotation. *Advances in Geocomputing*. Springer Berlin Heidelberg, Berlin, Heidelberg, 183-228.

Weatherley D, Hancock W, Boris V (2014) ESyS-Particle Tutorial and User's Guide Version 2.1. Earth Systems Science Computational Centre, The University of Queensland.

Wei D, Wang J, Nie J, Zhou B (2018) Generation of realistic sand particles with fractal nature using an improved spherical harmonic analysis. Comput Geotech 104: 1-12.

Wei H, Zan L, Li Y, Wang Z, Saxén H, Yu Y (2017) Numerical and experimental studies of corn particle properties on the forming of pile. Powder Technol 321: 533-543.

Xu Y, Dai F, Xu NW, Zhao T (2015) Numerical Investigation of Dynamic Rock Fracture Toughness Determination Using a Semi-Circular Bend Specimen in Split Hopkinson Pressure Bar Testing. Rock Mech Rock Eng 49(3): 731-745.

Yan P, Zhang J, Fang Q, Zhang Y (2018) Numerical simulation of the effects of falling rock's shape and impact pose on impact force and response of RC slabs. Constr Build Mater 160: 497-504.

Zhang L, Lambert S, Nicot F (2017a) Discrete dynamic modelling of the mechanical behaviour of a granular soil. Int J Impact Eng 103: 76-89.

Zhang L, Nguyen NGH, Lambert S, Nicot F, Prunier F, Djeran-Maigre I (2017b) The role of force chains in granular materials: from statics to dynamics. Eur J Environ Civ En 21(7-8): 874-895.

Zhang Y, Liu Z, Shi C, Shao J (2018) Three-dimensional Reconstruction of Block Shape Irregularity and its Effects on Block Impacts Using an Energy-Based Approach. Rock Mech Rock Eng 51(4): 1173-1191.

Zhao T, Dai F, Xu N (2017) Coupled DEM-CFD investigation on the formation of landslide dams in narrow rivers. Landslides 14(1): 189-201.

Zhao T, Dai F, Xu NW, Liu Y, Xu Y (2015) A composite particle model for non-spherical particles in DEM simulations. Granul Matter 17(6): 763-774.

Zhou Y, Wang H, Zhou B, Li J (2018) DEM-aided direct shear testing of granular sands incorporating realistic particle shape. Granul Matter 20(3): 55.

Captions

Fig. 1. (a) 3D laser scanner and (b) steps to reconstruct a realistic-shaped rock block.

Fig. 2. Numerical model configurations, (a) front view, (b) top view. The rock block is modeled as an assembly of bonded spherical particles, and the soil buffering layer is modeled as an assembly of polydisperse spherical particles obtained by gravitational deposition. The bulk density of the soil layer is 1514.9 kg/m^3.

Fig. 3. Different rock blocks used in the simulations (B-1, B-2, and B-3). The particles constituting rock blocks are colored based on their radii. L, I and S are the longest, intermediate and shortest principal geometric axes of the realistic-shaped rock block.

Fig. 4. Impact cases of the realistic-shaped rock block (B-2).

Fig. 5 Evolution of the acceleration of the rock block (B-1) in the experimental (Pichler et al. 2005) and numerical tests (h_f = 8.55 m).

Fig. 6. Comparisons between the numerical results in this study and the theoretical data in Pichler et al. (2005) for the cubic block impact: (a) maximum impact force, (b) final penetration depth.

Fig. 7 Evolution of the bottom center stress for the test of a spherical rock block with diameter of 0.9 m and mass of 850 kg impacting onto the soil layer at h_f = 36.5 m. The experimental results are those reported in Calvetti and di Prisco (2012).

Fig. 8. Evolution of the impact force (F_{block}) for the rock block (B-2) impacting against the soil layer with different impact surfaces (v_0 = 30 m/s) and for the spherical equal-volume (B-3).

Fig. 9. Evolution of the number of soil particles (N_{bc}) contacting with the realistic-shaped rock block (v_0 = 30 m/s).

Fig. 10. Dependence of the maximum impact force (F_{block}^{max}) on the impact velocity (v_0) for the rock block (B-2) and its equal-volume sphere (B-3). The solid lines are power-law fittings to the numerical data.

Fig. 11. Contact force chains formed in the soil layer at the time instant corresponding to the peak impact force for the realistic-shaped rock block impacting at v_0 = 30 m/s. Here, the force chain is defined as a network of straight lines connecting the centers of contacting particles. The thickness of these lines is proportional to the magnitude of contact force.

Fig. 12. Evolutions of the strain energy (a) and kinetic energy (b) of the soil particles for the rock block (B-2) impacting against the soil layer with different orientations (v_0 = 30 m/s).

Fig. 13. Evolution of the bottom force (F_{bott}) for the rock block (B-2) impacting against the soil layer with different orientations (v_0 = 30 m/s).

Fig. 14. Dependence of the maximum bottom force (F_{bott}^{max}) on the impact velocity (v_0) for the rock block (B-2) and its equal-volume sphere (B-3).

Fig. 15. Ratios of the maximum bottom force to the maximum impact force of rock block B-2 and B-3 impacting against the soil layer with various velocities.

Fig. 16. Discretization of the bottom floor for stress evaluation. The studied region, along the X and Y axial directions, is colored grey.

Fig. 17. Distribution of the peak normal stress along the X (a) and Y (b) axis of the bottom for the rock block (B-2) impacting against the soil layer at v_0 = 30 m/s.

Fig. 18. Relationship between the maximum stress ($\sigma_{x=0.0}^{max}$) acting on the bottom center (x = 0.0 m) and the impact velocity (v_0) for impacts of realistic-shaped rock block (B-2) and its equal-volume sphere (B-3).

Fig. 19. Relationship between the maximum stress ($\sigma_{x=0.0}^{max}$) acting on the bottom center and the maximum impact force (F_{block}^{max}) for the tests of rock blocks B-2 and B-3.

Fig. 20. Penetrating volume (PV) of rock blocks when assuming that the penetrating depth reaches one-tenth of the diameter of the equal-volume sphere (B-3).

Table 1. Input parameters used in the simulations. The particles densities in blocks B-1, B-2, B-3 are set differently so that the bulk density of rock block is 2700 kg/m^3.

Table 2. Impact velocity of rock block impact

Table 3 Ratio of the maximum impact force for B-2 to that for B-3 under condition of different impact velocities.

Table 4. Ratio of the maximum bottom force of B-2 to that of B-3 for different impact velocities.

Table 5 Amplification ratio of the soil layer for tests with B-2 and B-3 with various velocities.

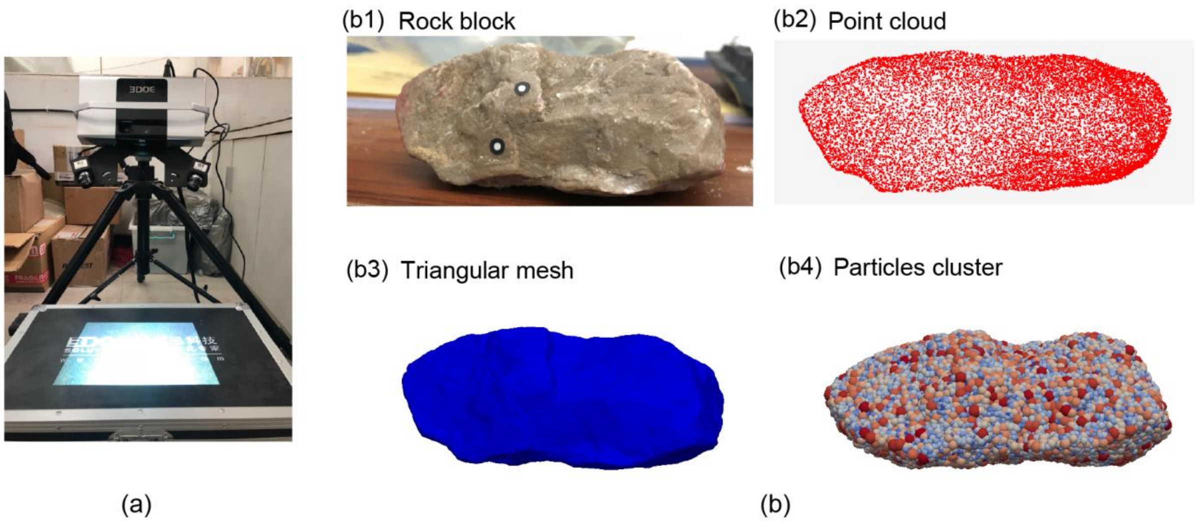

Fig. 1. (a) 3D laser scanner and (b) steps to reconstruct a realistic-shaped rock block.

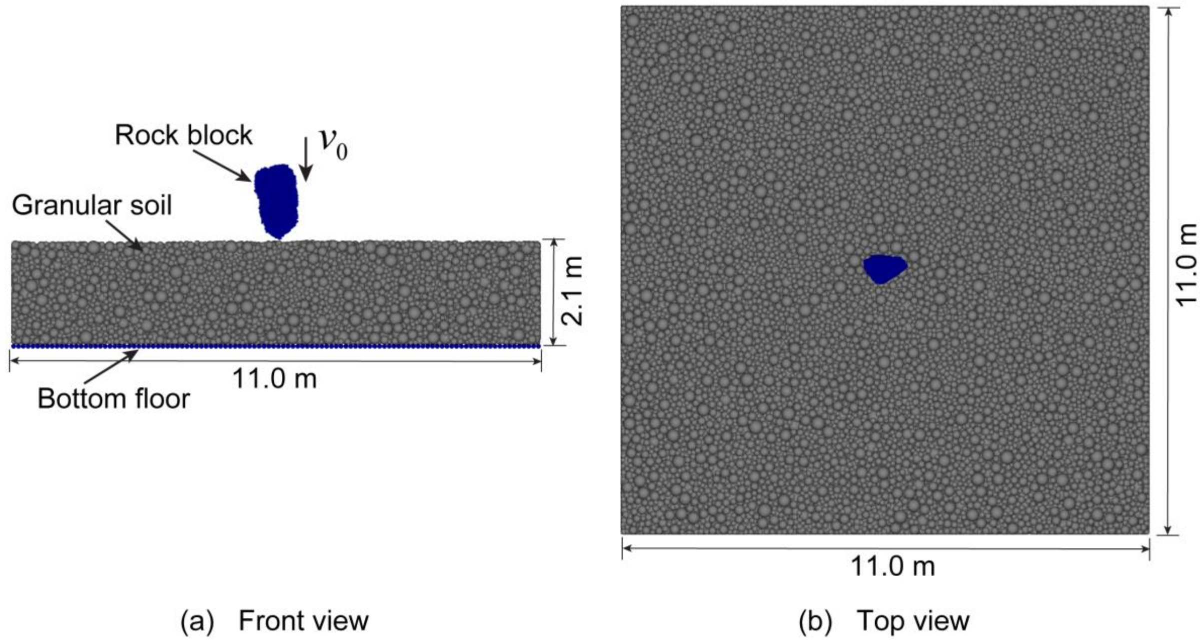

Fig. 2. Numerical model configuration, (a) front view, (b) top view. The rock block is modeled as an assembly of bonded spherical particles, and the soil buffering layer is modeled as an assembly of polydisperse spherical particles obtained by gravitational deposition. The bulk density of the soil layer is 1514.9 kg/m^3.

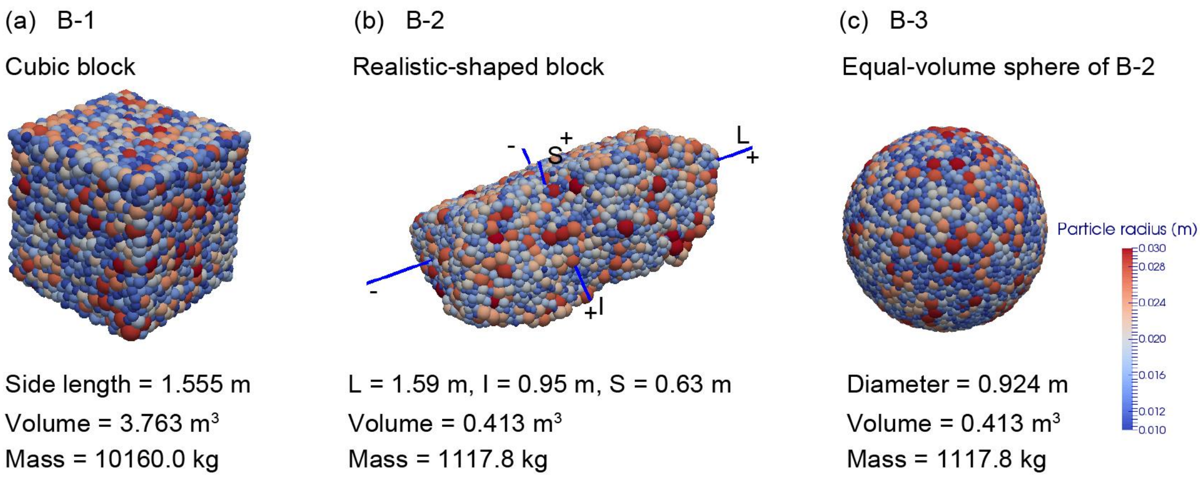

Fig. 3. Different rock blocks used in the simulations (B-1, B-2, and B-3). The particles constituting rock blocks are colored based on their radii. *L*, *I* and *S* are the longest, intermediate and shortest principal geometric axes of the realistic-shaped rock block.

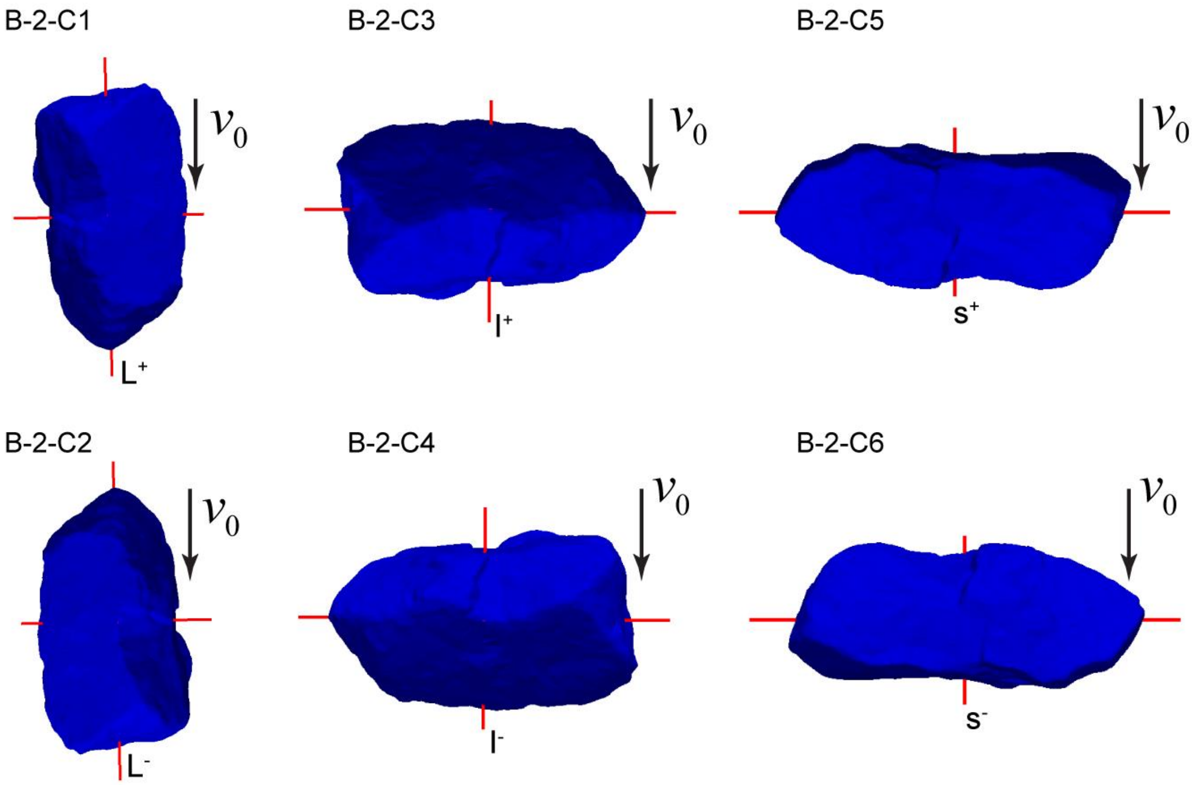

Fig. 4. Impact cases of the realistic-shaped rock block (B-2).

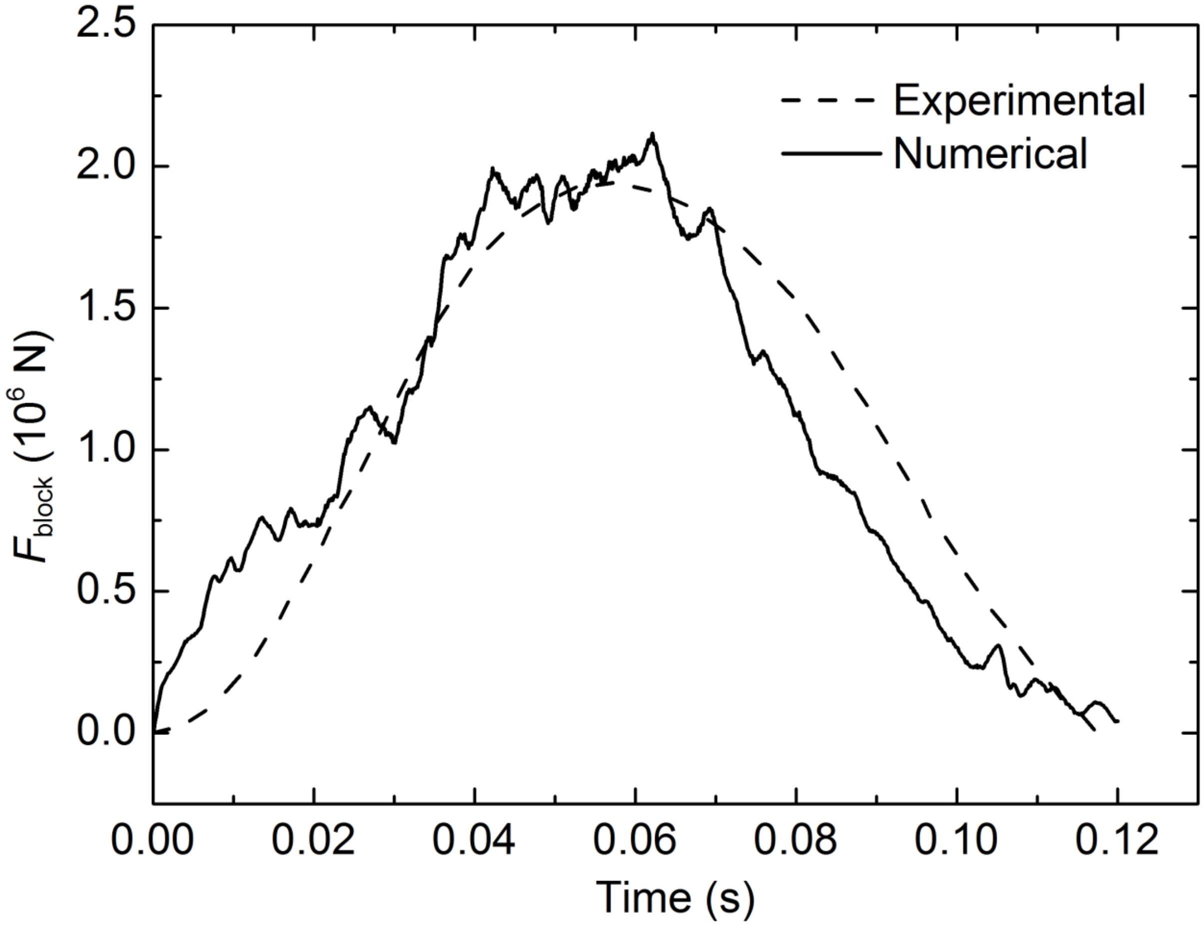

Fig. 5 Evolution of the impact force of the rock block (B-1) in the experimental (Pichler et al. 2005) and numerical tests (h_f = 8.55 m).

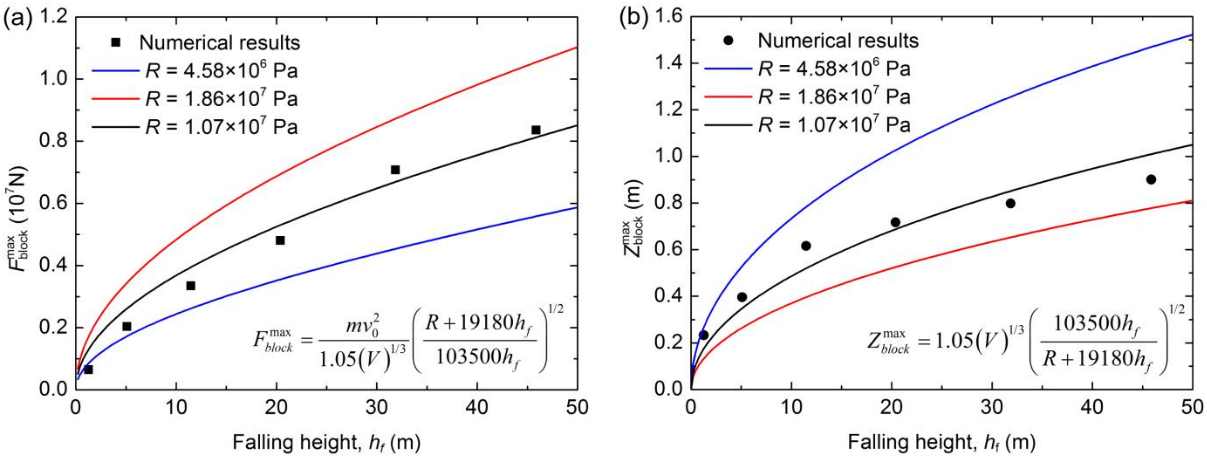

Fig. 6. Comparisons between the numerical results in this study and the theoretical data in Pichler et al. (2005) for the cubic block impact: (a) maximum impact force, (b) final penetration depth.

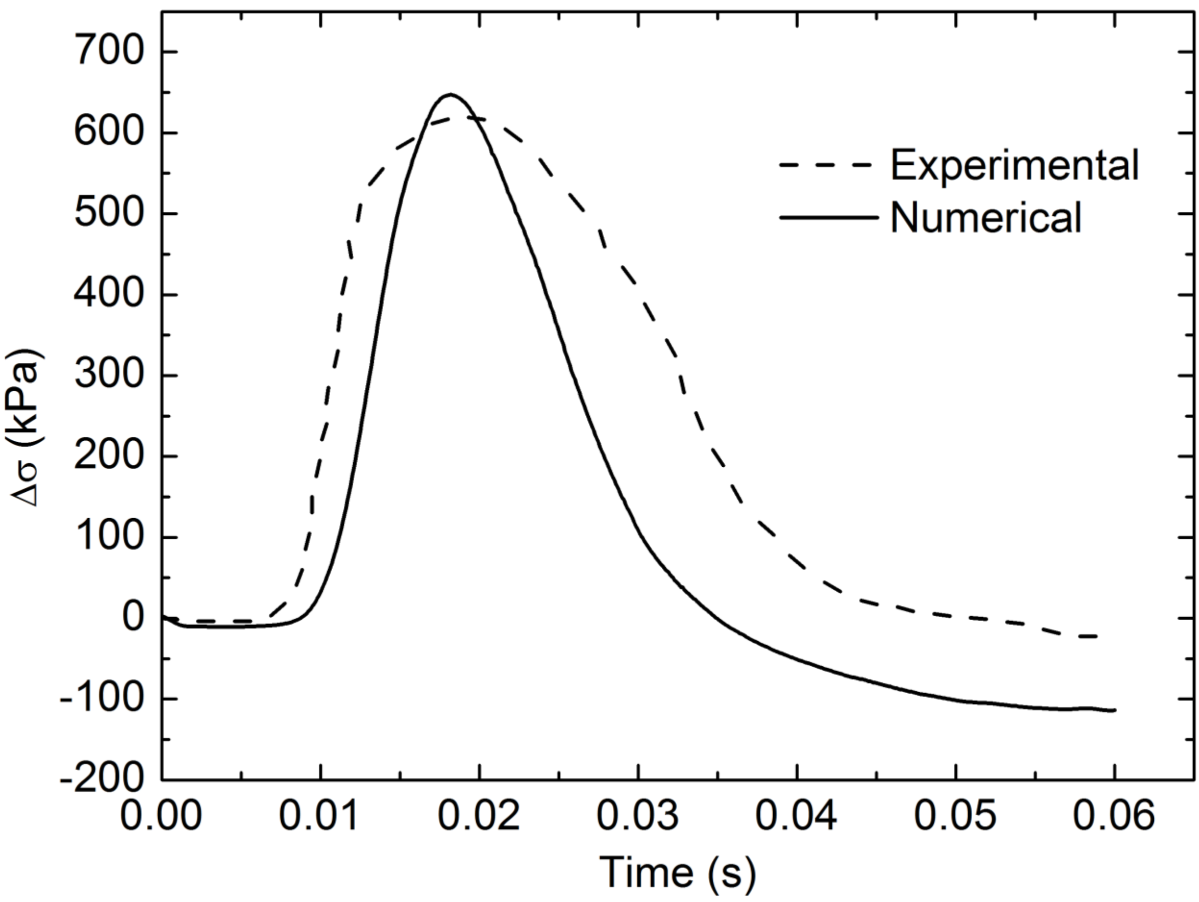

Fig. 7 Evolution of the bottom center stress for the test of a spherical rock block with diameter of 0.9 m and mass of 850 kg impacting onto the soil layer at h_f = 36.5. The experimental results is that reported in Calvetti and di Prisco (2012).

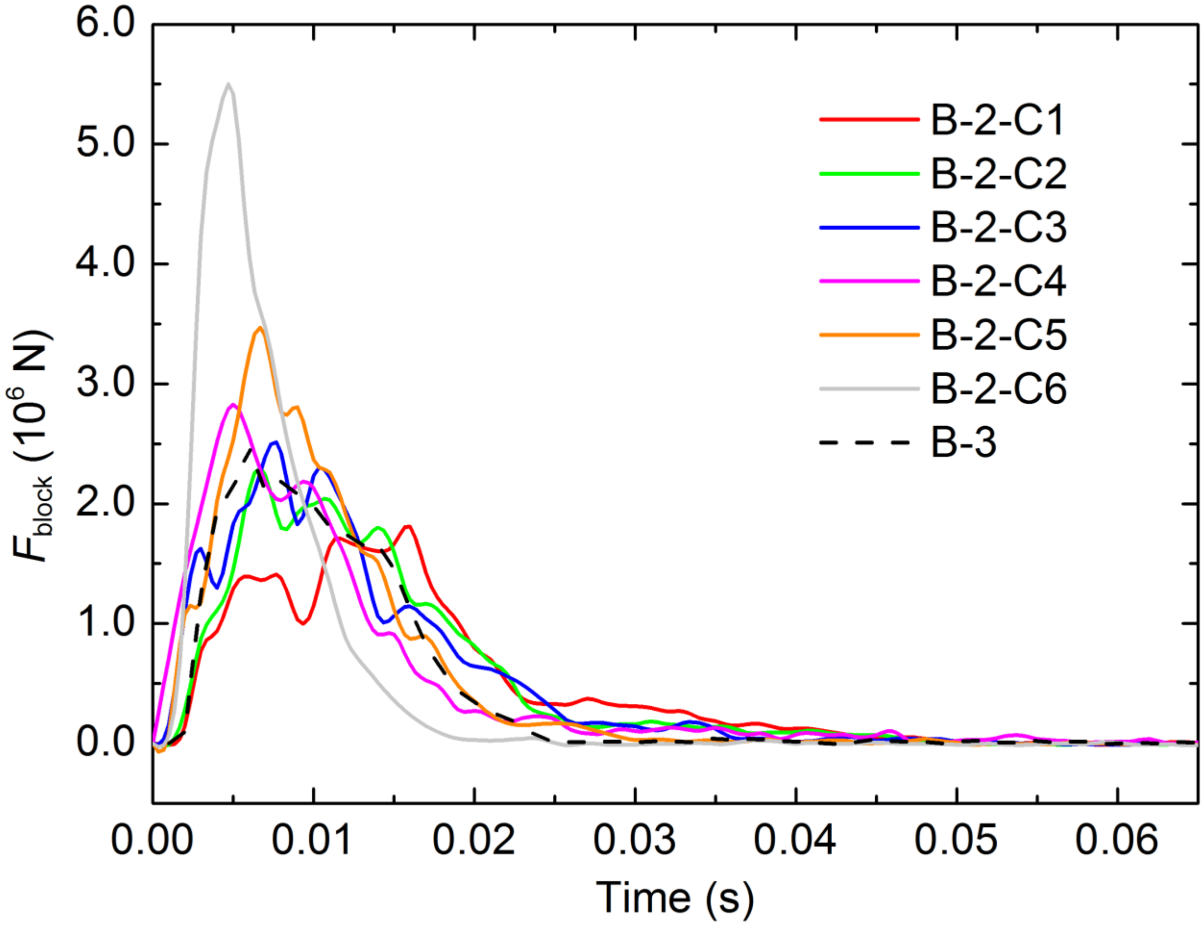

Fig. 8. Evolution of the impact force (F_{block}) for the rock block (B-2) impacting against the soil layer with different impact surfaces (v_0 = 30 m/s) and for the spherical equal-volume (B-3)

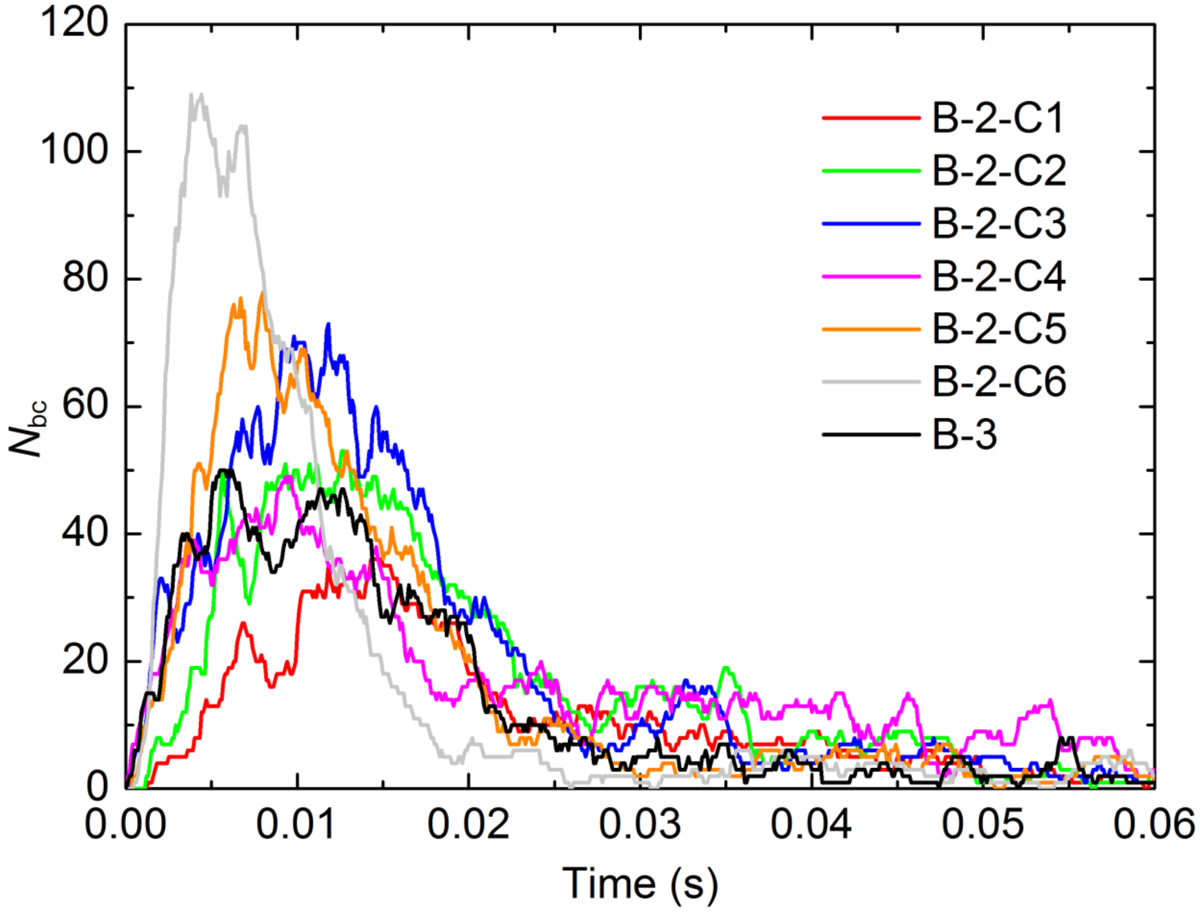

Fig. 9. Evolution of the number of soil particles (N_{bc}) contacting with the realistic-shaped rock block (v_0 = 30 m/s).

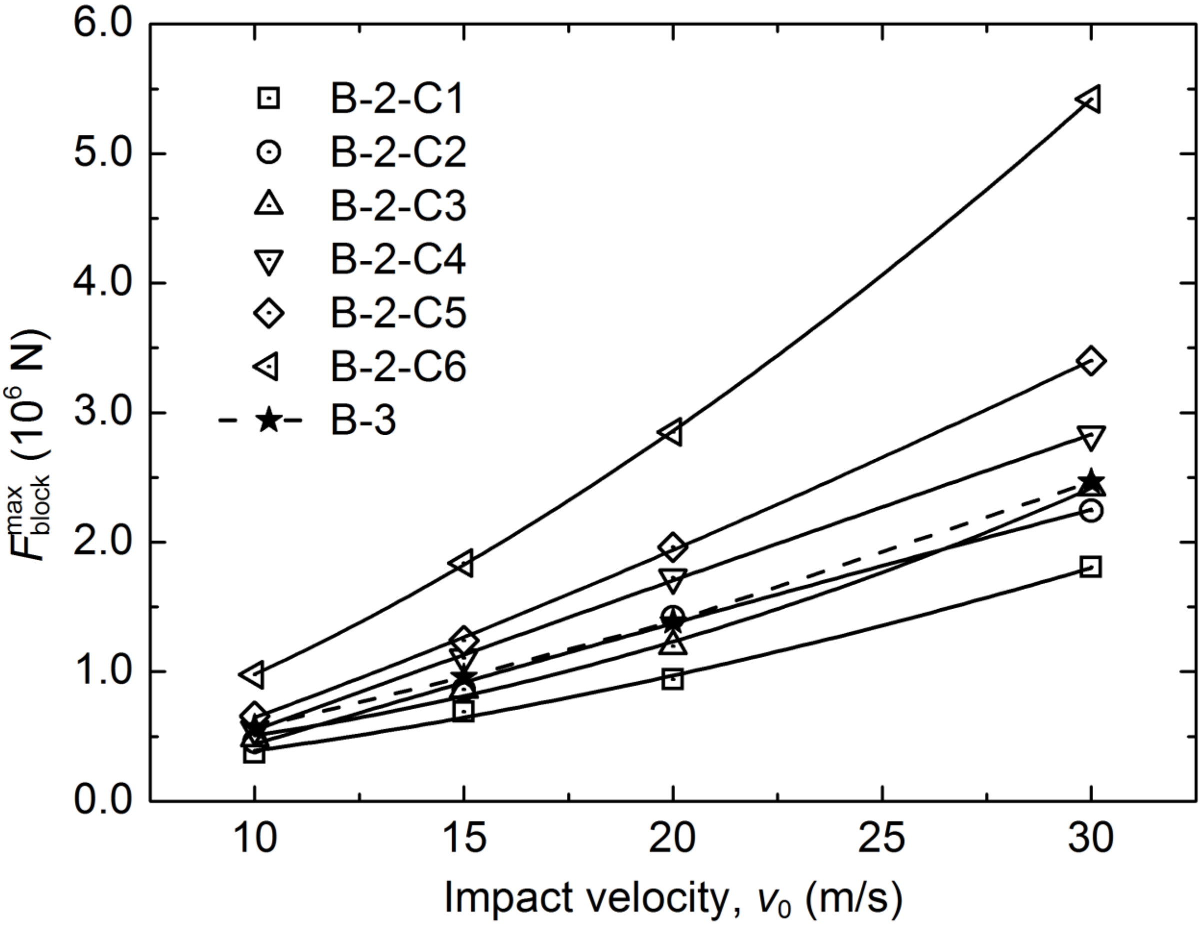

Fig. 10. Dependence of the maximum impact force (F_{block}^{max}) on the impact velocity (v_0) for the rock block (B-2) and its equal-volume sphere (B-3). The solid lines are power-law fittings to the numerical data.

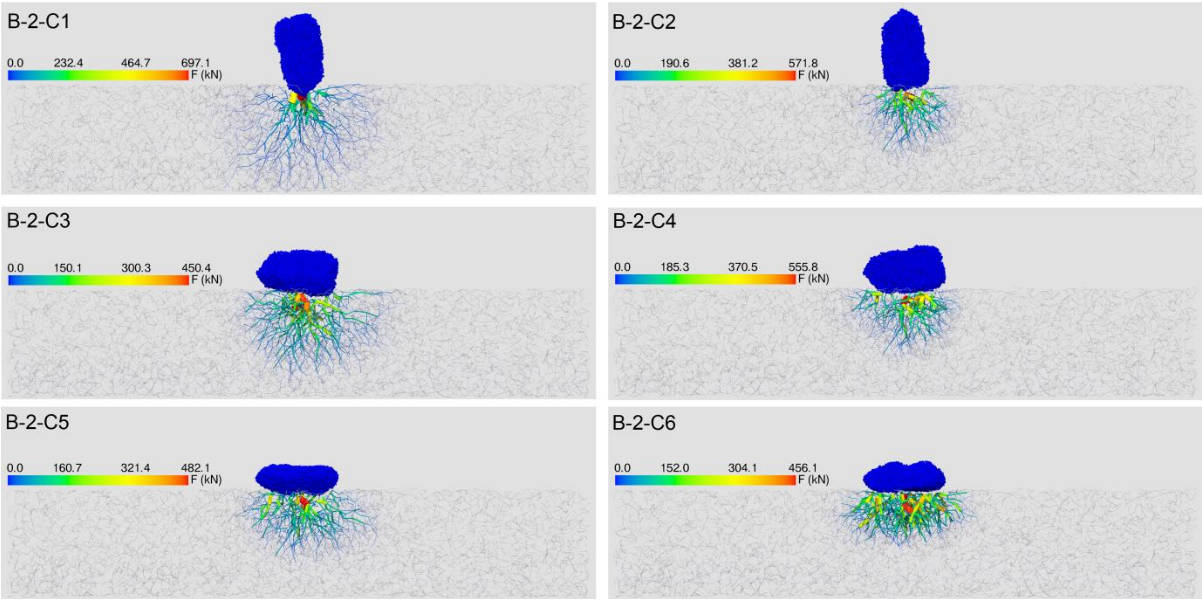

Fig. 11. Contact force chains formed in the soil layer at the time instant corresponding to the peak impact force for the realistic-shaped rock block impacting at v_0 = 30 m/s. Here, the force chain is defined as a network of straight lines connecting the centers of contacting particles. The thickness of these lines is proportional to the magnitude of contact force.

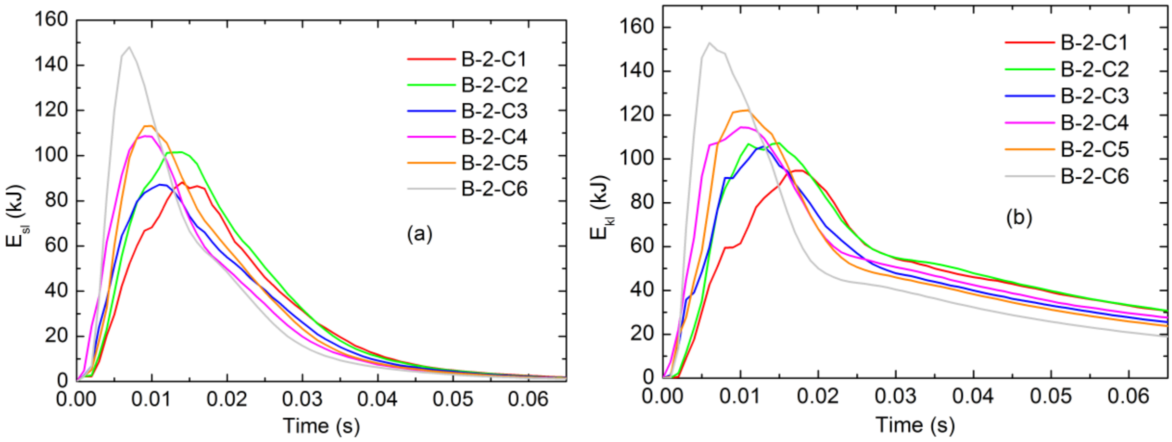

Fig. 12. Evolutions of the strain energy (a) and kinetic energy (b) of the soil particles for the rock block (B-2) impacting against the soil layer with different orientations (v_0 = 30 m/s).

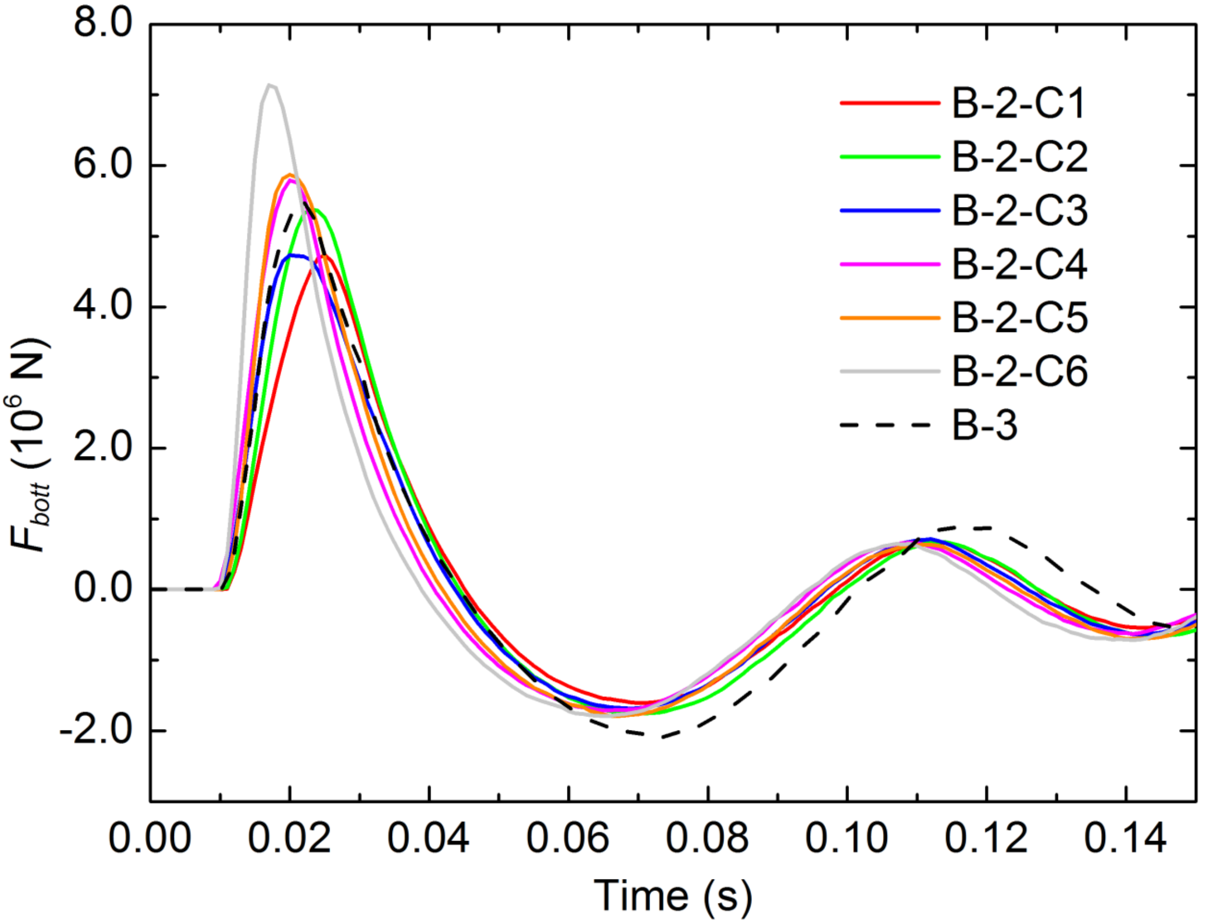

Fig. 13. Evolution of the bottom force (F_{bott}) for the rock block (B-2) impacting against the soil layer with different orientations (v_0 = 30 m/s).

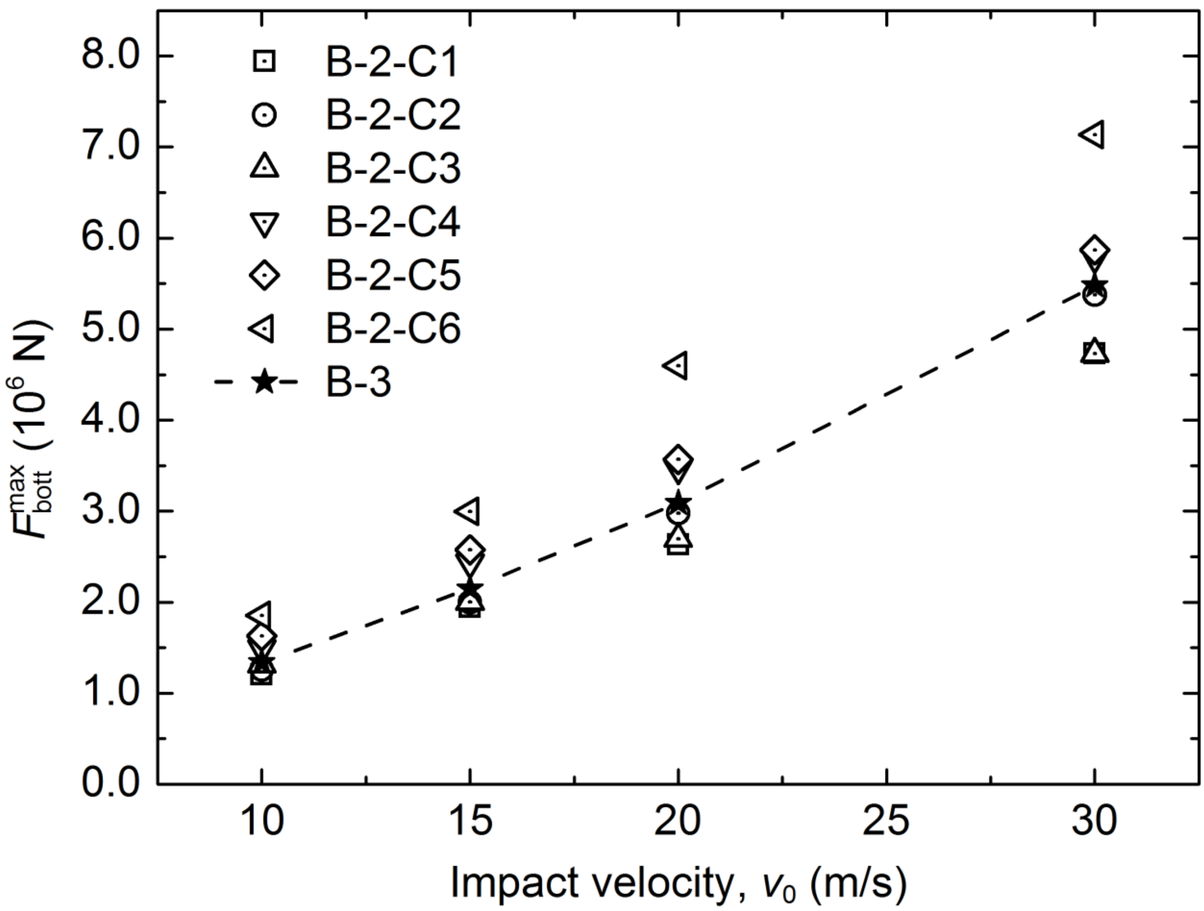

Fig. 14. Dependence of the maximum bottom force (F_{bott}^{max}) on the impact velocity (v_0) for the rock block (B-2) and its equal-volume sphere (B-3).

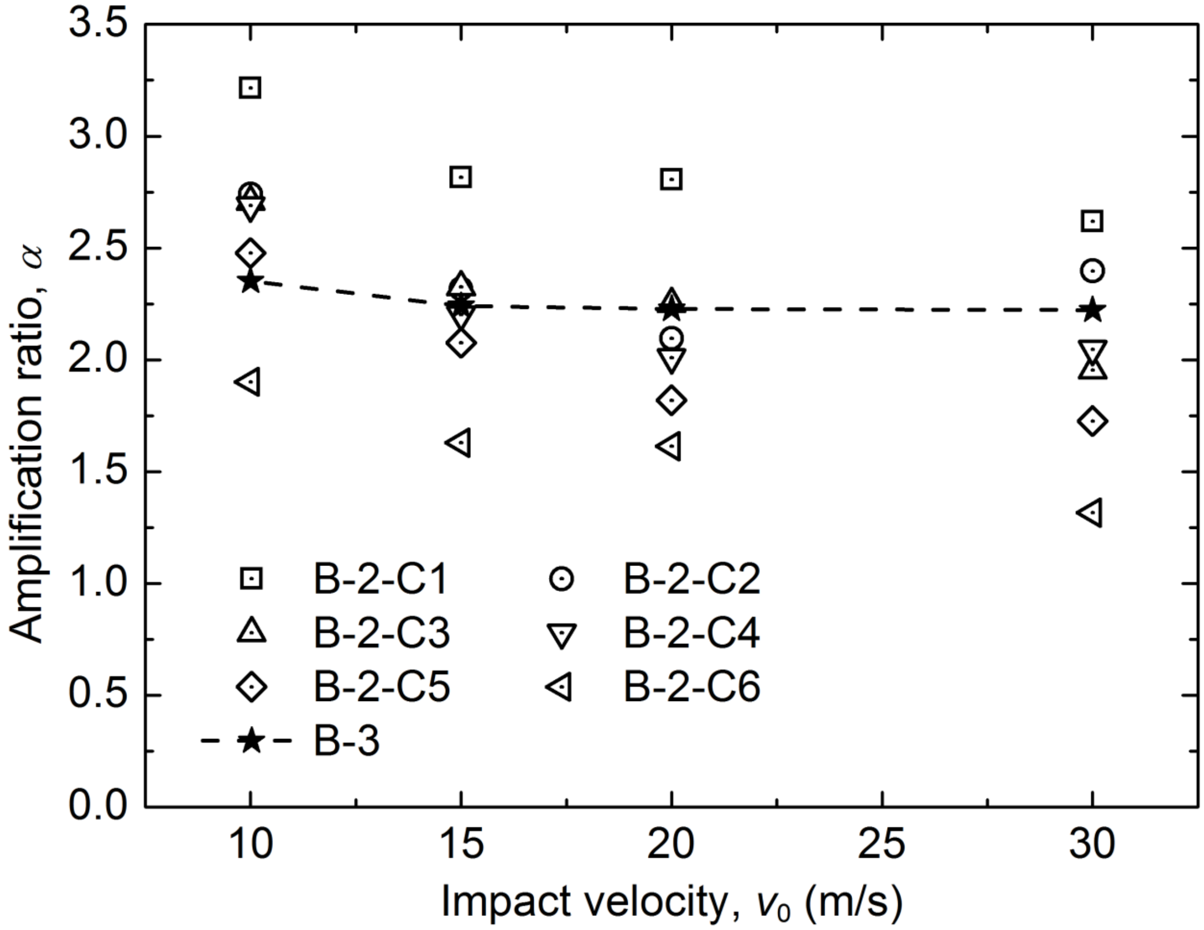

Fig. 15. Ratios of the maximum bottom force to the maximum impact force of rock block B-2 and B-3 impacting against the soil layer with various velocities.

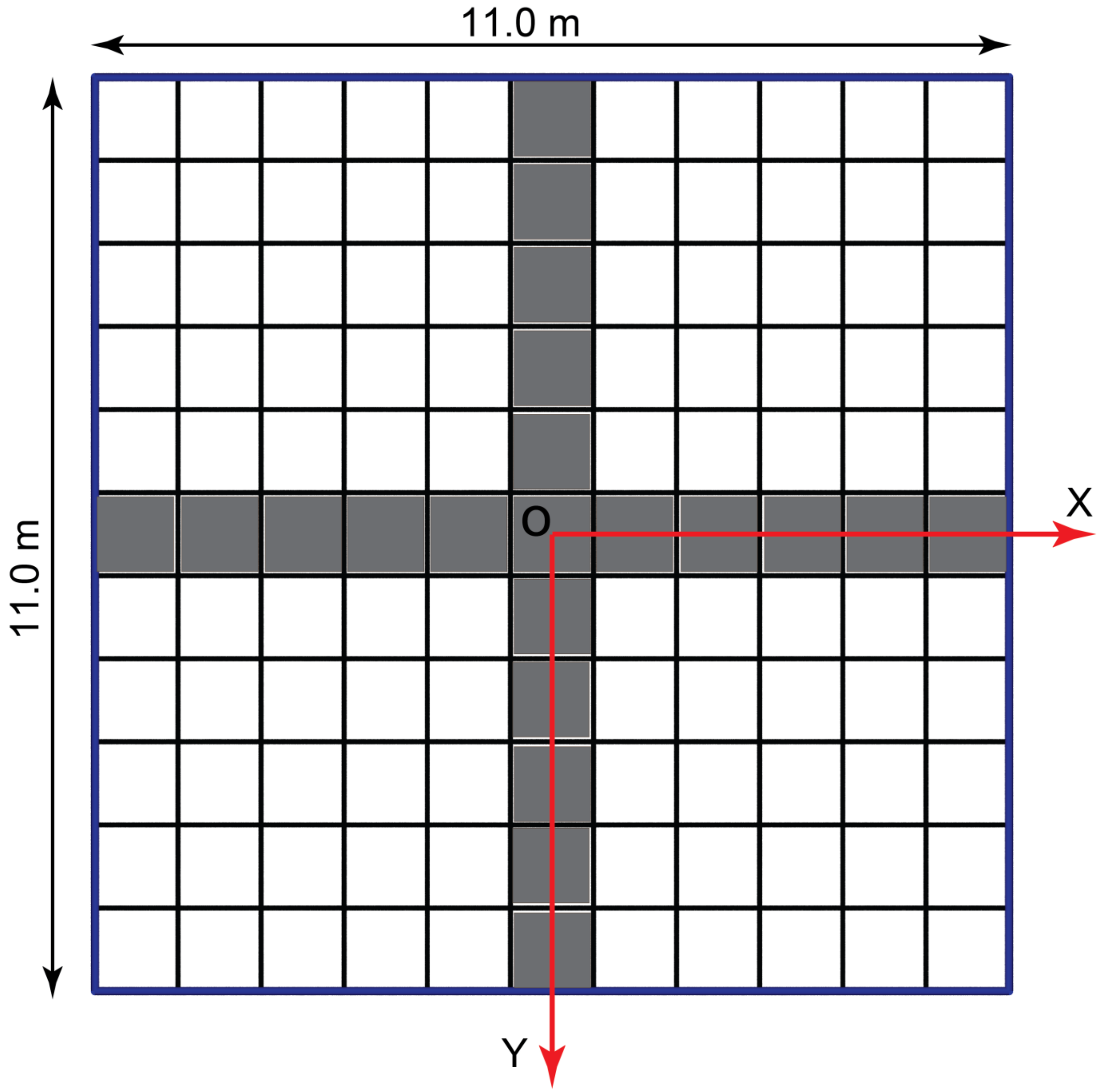

Fig. 16. Discretization of the bottom floor for stress evaluation. The studied region, along the X and Y axial direction, is colored grey.

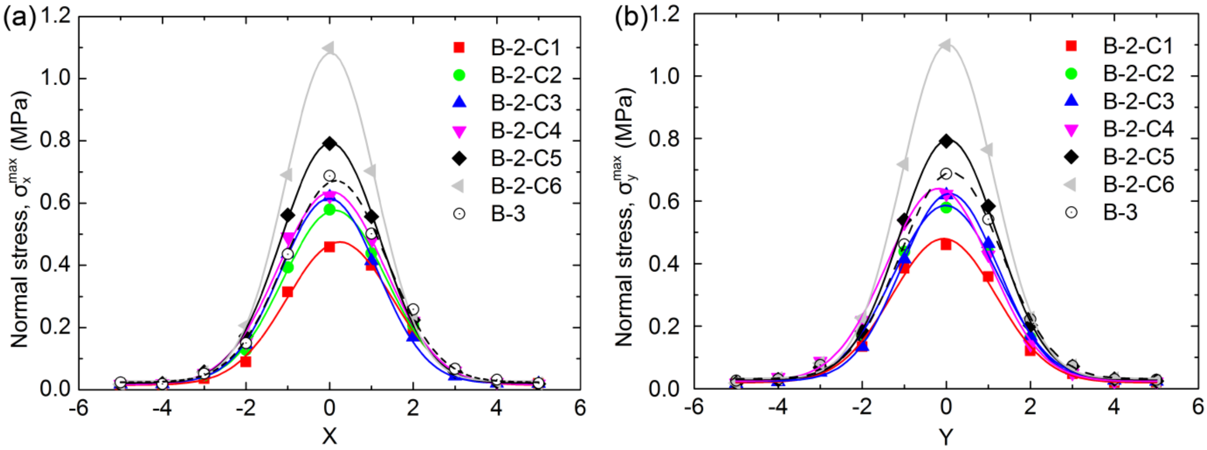

Fig. 17. Distribution of the peak normal stress along the X (a) and Y (b) axis of the bottom for the rock blocks (B-2) and (B-3) impacting against the soil layer at v_0 = 30 m/s.

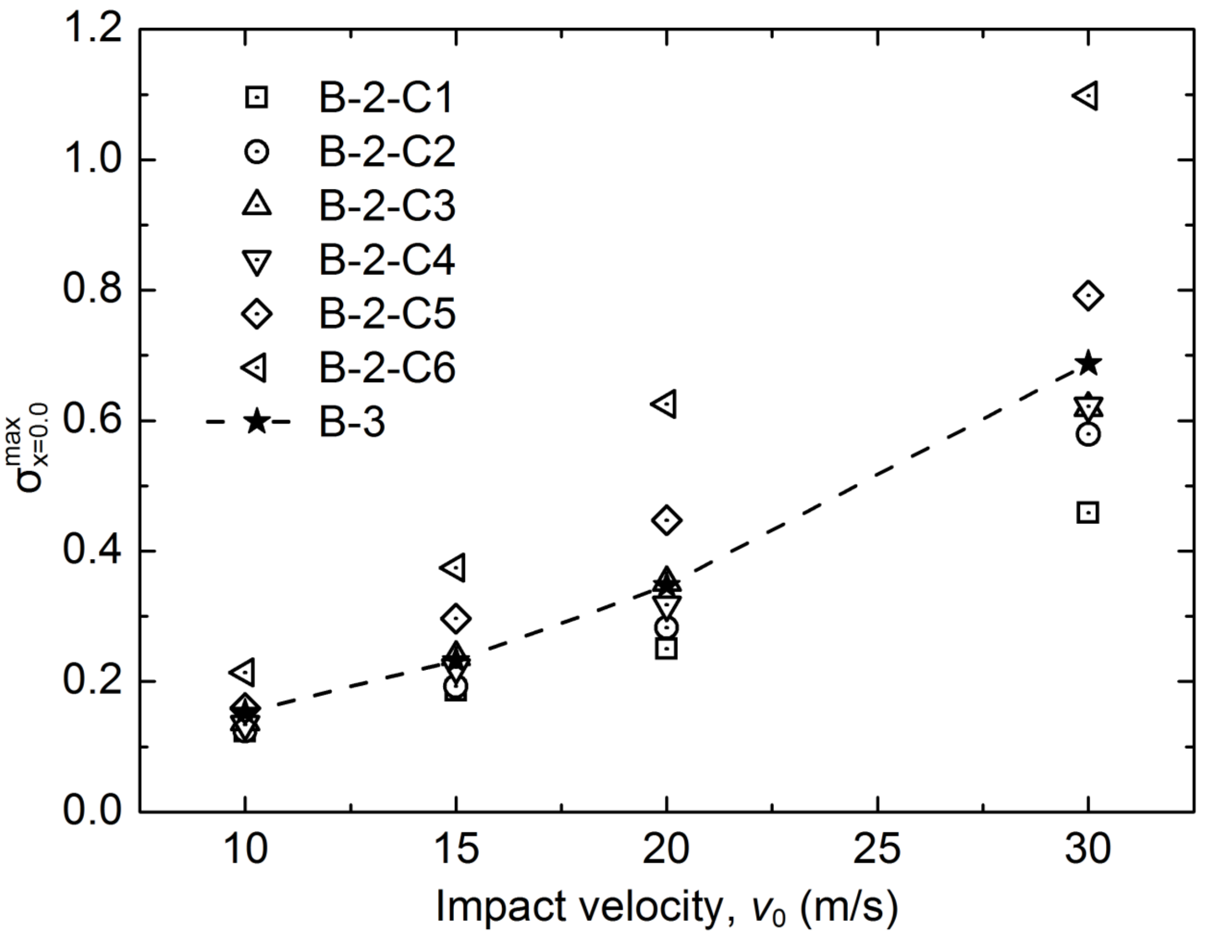

Fig. 18. Relationship between the maximum stress ($\sigma_{x=0.0}^{max}$) acting on the bottom center (x = 0.0 m) and the impact velocity (v_0) for impacts of realistic-shaped rock block (B-2) and its equal-volume sphere (B-3).

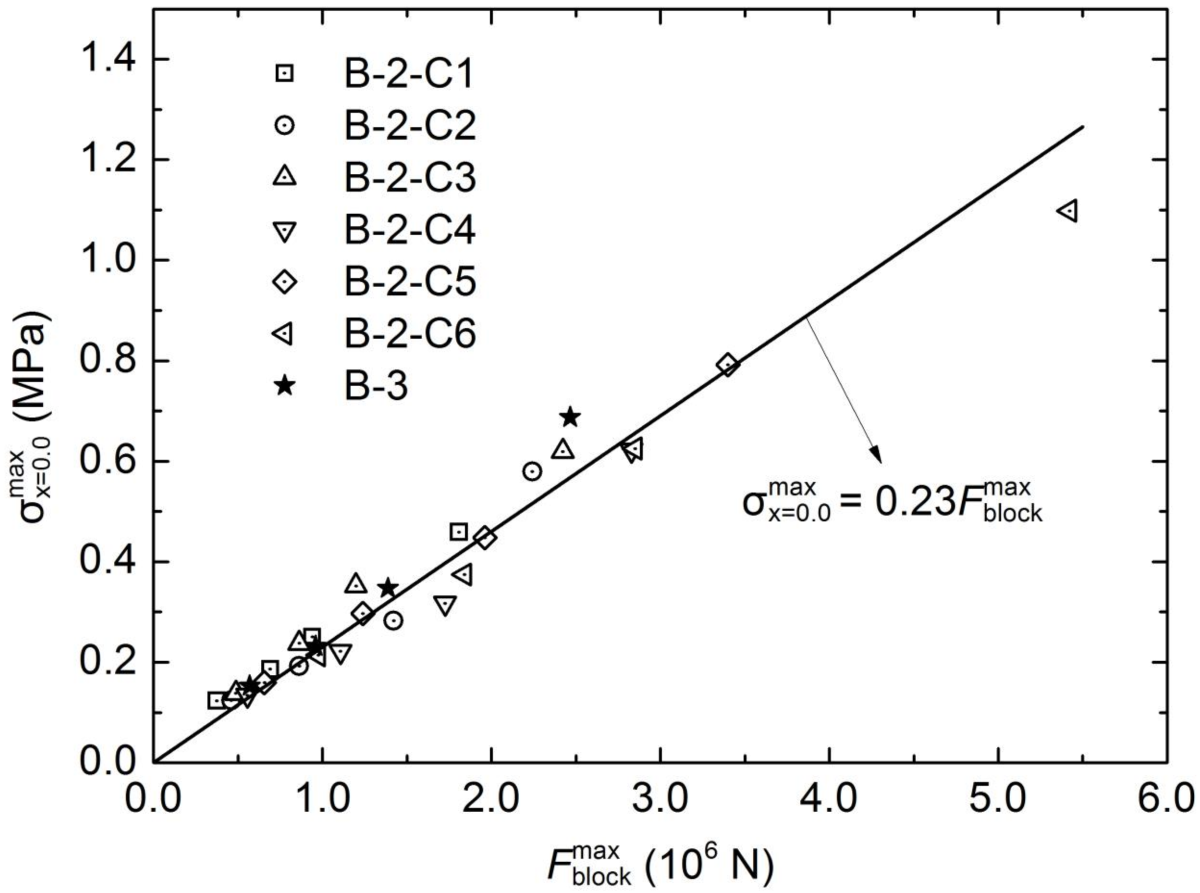

Fig. 19. Relationship between the maximum stress ($\sigma_{x=0.0}^{max}$) acting on the bottom center and the maximum impact force (F_{block}^{max}) for the tests of rock blocks B-2 and B-3.

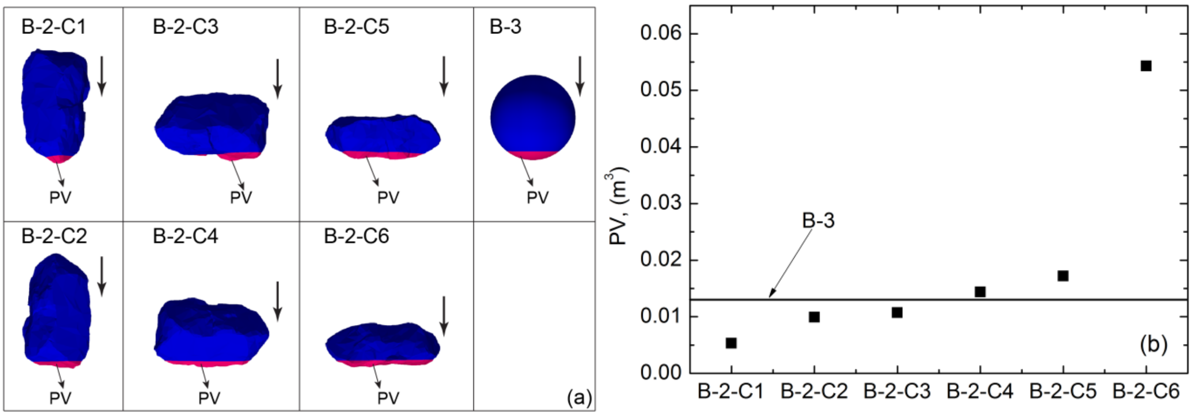

Fig. 20. Penetrating volume (PV) of rock blocks when assuming that the penetrating depth reaches one-tenth of the diameter of the equal-volume sphere (B-3).

Table 1. Input parameters used in the simulations. The particles densities in blocks B-1, B-2, B-3 are set differently so that the bulk density of rock block is 2700 kg/m^3.

DEM parameters	Value	DEM parameters	Value
Soil particle radius (m)	0.05-0.15	Young's modulus of particle, E_p (MPa)	1×10^2
Slab particle radius (m)	0.05	Particle Poisson's ratio, υ	0.25
Block particle radius (m)	0.01-0.03	Viscous damping coefficient, β	0.01
B-1 particle density (kg/m^3)	5242.6	Particle friction coefficient, μ	0.577
B-2 particle density (kg/m^3)	5063.8	Cohesion of bonds, c (MPa)	1×10^{20}
B-3 particle density (kg/m^3)	4461.5	Young's modulus of bonds, E_b (MPa)	1×10^4
Soil particle density, ρ (kg/m^3)	2650.0	Gravitational acceleration, g (m/s^2)	9.81
Slab particle density (kg/m^3)	2650.0	Time step size, Δt (s)	1×10^{-6}

Table 2. Initial impact velocity of rock block impact

Vertical velocity, v_0 (m/s)	Equivalent falling height, h_f (m)
10.0	5.1
15.0	11.5
20.0	20.4
30.0	45.9

Table 3 Ratio of the maximum impact force for B-2 to that for B-3 under condition of different initial impact velocities.

v_0 (m/s)	B-2-C1	B-2-C2	B-2-C3	B-2-C4	B-2-C5	B-2-C6
10.0	0.66	0.81	0.86	0.98	1.15	1.71
15.0	0.72	0.90	0.90	1.15	1.29	1.92
20.0	0.68	1.02	0.86	1.24	1.41	2.06
30.0	0.73	0.91	0.98	1.15	1.38	2.20

Table 4. Ratio of the maximum bottom force of B-2 to that of B-3 for different initial impact velocities.

v_0 (m/s)	B-2-C1	B-2-C2	B-2-C3	B-2-C4	B-2-C5	B-2-C6
10.0	0.90	0.94	0.98	1.12	1.22	1.39
15.0	0.91	0.93	0.93	1.13	1.20	1.40
20.0	0.85	0.96	0.87	1.12	1.16	1.49
30.0	0.86	0.98	0.86	1.06	1.07	1.30

Table 5 Amplification ratio of the soil layer for tests with B-2 and B-3 with various velocities.

v_0 (m/s)	B-2-C1	B-2-C2	B-2-C3	B-2-C4	B-2-C5	B-2-C6	B-3
10	3.22	2.74	2.71	2.69	2.48	1.90	2.35
15	2.82	2.32	2.33	2.20	2.08	1.63	2.24
20	2.81	2.10	2.25	2.01	1.82	1.61	2.23
30	2.62	2.40	1.95	2.05	1.73	1.32	2.22